Microstructural examination of neutron, proton and self-ion irradiation damage in a model Fe9Cr alloy

J. C. Haley[a+], S. de Moraes Shubeita[b], P. Wady[b], A.J. London[c], G. R. Odette[d], S. Lozano-Perez [a], S. G. Roberts [a]

[a]*Department of Materials, University of Oxford, Parks Road, Oxford, OX1 3PH, United Kingdom*
[b]*Dalton Cumbrian Facility, University of Manchester, Westlakes Science Park, Moor Row, Cumbria CA24 3HA, UK*
[c]*CCFE, UK Atomic Energy Authority, Culham Science Centre, Abingdon, Oxfordshire OX14 3DB, United Kingdom*
[d]*UCSB Department of Mechanical Engineering, 2343 Engineering II Building, Santa Barbara, CA 93106-5070, USA*

Abstract

Transmission electron microscopy (TEM) was used to compare the microstructural defects produced in an Fe9Cr model alloy during exposure to neutrons, protons, or self-ions. Samples from the same model alloy were irradiated using fission-neutrons, 2MeV Fe+ ions or 1.2MeV protons at similar temperatures (~300°C) and similar doses (~2.0dpa). The neutron-irradiated alloy contained visible interstitial dislocation loops with **b**=⟨111⟩, and on average ~5nm in size. The density varied from $2\pm1\times10^{20}$ m^{-3} (in the matrix far from dislocations and boundaries) to $1.2\pm0.3\times10^{23}$ m^{-3} (close to helical dislocation lines). Chromium α'-phase precipitates were also identified at a density of $7.4\pm0.4\times10^{23}$ m^{-3}. Self-ion irradiation produced mostly homogeneously distributed dislocation loops (6-7nm on average), and with a greater fraction of ⟨100⟩ loops (~40%) than was seen in the neutron-irradiated alloy, and at a density of $6.8\pm0.8\times10^{22}$ m^{-3}. In contrast to the loops produced by neutron irradiation, the self-ion irradiated Fe9Cr contained only vacancy-type loops. Chromium also remained in solution. Proton-irradiated Fe9Cr contained interstitial dislocation loops close to helical-dislocation segments, similar to the neutron-irradiated sample. Chromium α'-phases were also identified in the proton-irradiated sample at a density of $2.5\pm0.3\times10^{23}$ m^{-3}, and large voids (up to 7nm) were found at a density over $10^{22}m^{-3}$. Like the neutron-irradiated sample, the density of dislocation loops was also heterogeneously distributed; far from grain boundaries and dislocation lines the density was $2.5\pm0.4\times10^{22}$ m^{-3}, while close to helical dislocation lines the density was $8.1\pm1.3\times10^{22}$ m^{-3}.

Key words: radiation damage; proton irradiation; ion irradiation; TEM

[+] *Corresponding author: jack.haley@materials.ox.ac.uk (J. Haley)*

Second draft 01/04/2020

1 – Introduction

Replicating the radiation damage that occurs in structural materials exposed to nuclear reactor conditions – fission or fusion – is essential for understanding their performance during operation and predicting component lifetimes before catastrophic failure can occur. A sustained high flux of fission- or fusion-spectrum neutrons will disrupt the ordered microstructure of a material via the creation of defects (for example; dislocation loops, precipitates, cavities and bubbles, and grain boundary segregation) leading to radiation hardening and embrittlement [1].

Charged particles have a long history of use as a means for creating damage similar to that produced by neutrons in a nuclear reactor [2,3], and enable experiments to be conducted under a more controlled environment and with easier access for researchers than nuclear reactor-based experiments. Heavy-ions can produce high doses of radiation damage much faster than neutrons, allowing doses that might require a year or (several) in a reactor to be achieved in mere hours or days. A further advantage is that the ion energies typically used (from keV up to a few 10s of MeV) are too low to cause any transmutation reactions, and thus materials do not become radioactive from the process. This greatly simplifies the analysis post-irradiation.

Though being able to implant high neutron-equivalent damage doses in a matter of hours rather than months/years is advantageous, the rate at which damage is implanted changes how the defects evolve and interact with sinks (grain boundaries, dislocations etc.) [4,5]; this is the dose-rate effect. This disadvantage of charged particle irradiation can cause significantly different damage and hardening of a material for equivalent dose irradiations [6–8].

A further disadvantage of heavy-ion irradiation is that the damage produced is contained within only a few microns (at best) from the surface of the material. Measurements of mechanical properties from small volumes is very difficult; micromechanical tests (for example, nanoindentation [9,10], micro-cantilever testing [10,11], micro-tensile testing [12,13], and micro-pillar compression

[14]) are required to characterise the mechanical changes due to heavy-ion damage. Such tests are difficult to prepare reliably, and so many repeats are usually required to account for the variability of the measurement. Furthermore, with a reduction in probed volume comes an increase in the apparent strength of a material. This is the so-called “size effect” which can make results from these small-scale tests unrepresentative of the bulk mechanical properties [11]. This is significant for the <5μm depths of typical heavy ion-irradiated layers in ferritic alloys and steels [11,15].

Protons are seen as an alternative to heavy-ions for charged particle irradiations, since for equivalent energies they penetrate much further (typically tens of microns) into the sample than heavy ions. Though micromechanical techniques are still a requirement, they can be conducted on larger volumes, where the tests are less variable and size effects are less significant [11,15]. Furthermore, the damage profile produced by protons is much smoother prior to the Bragg peak for equivalent damage depths, which greatly simplifies the analysis since there will be less depth-dependent hardening. However, the dose rate for proton-irradiation is typically an order of magnitude or more lower than for heavy-ion irradiation; this increases the time required to reach significant (>1 dpa) dose levels.

Was et al. [16] highlighted the advantages of proton irradiation and showed that it can be effective at recreating many aspects of neutron damage. They compared austenitic RPV cladding steels (304SS and 316SS) that were irradiated with neutrons up to a dose of 5 displacements per atom (dpa) at 275°C, with the same heat samples irradiated with 3.2 MeV protons to the same dose but at a higher temperature of 360°C. The 85°C shift in temperature was used to counteract differences in the microstructure due to the differences in dose rate effect between neutron and proton irradiation ($7x10^{-6}$ dpa/s and ~10^{-8}-10^{-7} dpa/s), as proposed by Mansur et al. [5].

Was et al. [16] found many aspects of the neutron irradiation damage in steel were replicated well by the proton irradiation. The spatial extent of radiation-induced segregation (RIS) at grain

boundaries, the hardening, and the defect types and densities were all similar; this proof of principle study has led to a large number of proton irradiation studies. These include studies of radiation-induced interstitial/vacancy defect clusters [17–22], precipitation [21–25] and segregation [18,19,22,26], and mechanical changes [15,20,22–24,27]; irradiation assisted stress corrosion cracking has also been studied extensively using proton irradiation [22,28,29]. Studies have also continued to compare proton irradiation to neutron irradiation experiments [17,22].

While much is known about the nature of charged particle irradiation, there are important avenues that have not been explored in detail. Firstly, while there are examples where self-ion [7,11] or proton irradiation [16,17,22] have been compared with neutrons, few have compared both self-ion *and* proton irradiation with neutrons, and none in model alloys with clean initial microstructures. Furthermore, the effects of protons and self-ions have not been compared at the same displacement dose-rate and same temperature. This is important to study, since protons and heavy-ions generate very different recoil spectra, which affects the defect survival rate and the number of freely migrating defects (which in turn affects the diffusion rate of alloyed elements)

Swenson and Wharry [17,30] analysed neutron, proton and self-ion irradiated commercial ferritic martensitic steels (HCM12A and HT9) and model Fe9Cr ODS alloy irradiated at 500°C. In this study, they looked at ODS nanocluster evolution, radiation induced precipitation, and dislocation loop evolution. They found dislocation loop sizes and densities correlated well after irradiation to 3 dpa by each particle, partly due to saturation being reached and the high initial sink density.

Protons typically produce small cascades, with a high efficiency for defect survival after a cascade cools (approx. 60-120% of the standard Norgett, Robinson and Torrens (NRT) dpa) [31]. Self-ions produce large cascades close together with a lower efficiency for defect survival (~30% of the NRT-dpa) [31] and similar to neutron-induced cascades; large cascades are also more likely to split into many sub-cascades and form large defect clusters [32]. Use of self-ion irradiation to reproduce

the effects of neutron irradiation has often been justified as giving an accurate reproduction of the neutron recoil spectra as long as sub-cascade splitting occurs, since the size distribution of discrete sub-cascade volumes will saturate when sub-cascade branching dominates [33]. This means that if the implanted ion is energetic enough to create a cascade that branches into discrete sub-cascades, the implanted ion can be thought of as the primary knock-on atom of a neutron-induced cascade and thus the defect structures that form should be the same; this would not be expected of proton irradiation in the typically-used few-MeV range.

Although small errors in the dose rate do not greatly affect the Mansur [5] temperature shift (for compensating dose-rate differences), we note that irradiations using protons are rarely conducted at the same temperature as the neutron irradiation being emulated [17]. Thus, the benefits of such a dose-rate compensating temperature shift are not always clear, despite them being widely used. This is especially important in the study of ferritic alloys/steels, since the Mansur temperature shifts do not consider temperature-dependent traits of certain defects, such as the stability of cluster types. For example, it is well known that immobile $\langle 100 \rangle$-type dislocation loops in ferritic materials are more stable at higher temperatures than the mobile $\langle 111 \rangle$ loops [34], leading to abrupt changes in the defect morphology between 300°C and 400°C [35]. Another example is the precipitation of chromium-rich α'-phases, which shift in stability between 300°C and 400°C according to the Fe-Cr phase diagram [36,37].

Swenson and Wharry [30,38] irradiated commercial ferritic-martensitic steels and model Fe9Cr ODS alloy using neutrons, protons and self-ions at the same temperature, but with dose-rates spanning 4 orders of magnitude. They showed how due to radiation-enhanced diffusion, some surrogate particle irradiations may be better suited to a negative temperature shift, as has also been suggested by Martin [39]; this opposes the Mansur approach of a positive temperature shift to offset dose rate. This effect of radiation enhanced diffusion would be particularly important for proton

irradiation, where the fraction of freely migrating defects produced is high, but less so for self-ion irradiation where segregation and precipitation can be disrupted by the frequent large cascades [40].

Temperature shifts to offset dose-rate effects have been shown to work to some degree; however, we find that dose calculations can be inconsistent across studies. For example, Was et al. [16] notes that the dose they used to calculate displacements per atom (dpa) for their proton irradiation used a displacement energy of 25eV, rather than the accepted value of 40eV [41]. While this makes little difference to the temperature shift, it does mean the proton NRT-dose used by Was et al. is nearly twice that of their neutron irradiation. The calculated temperature shift also does not account for differences in cascade efficiency, so the defect production rate is unaccounted for.

Further complications for displacement calculations were highlighted by Stoller et al. [42], who noted that the "Full Cascade" mode in SRIM [43] actually overestimates the NRT-model vacancy production rate by roughly a factor of two. Stoller et al. recommended avoiding use of the vacancy production rate calculated by "Full-Cascade" SRIM due to these discrepancies; instead, the damage energy should be calculated from the SRIM energy partition outputs of SRIM's "Quick K-P" model by converting these to an atomic displacement rate via the NRT equation [42,44]. It is unclear whether these latter points affect Was et al.'s study [16], but they do highlight the need for consistency and rigour in reporting SRIM calculations, and cast uncertainty over many studies that compare charged particles to neutrons. However, the important finding of Was et al.'s study [16] is not necessarily that equivalent dose neutron and proton irradiation yields equivalent damage – more that there is a calculable dose dependency between the two.

The aim of the study reported here was to provide insight into the differences in damage produced by neutron and charged particle irradiations when the irradiation conditions (temperature and NRT-dpa) are matched as closely as possible. Specifically, we compare neutron, proton and self-

ion damage within the exact same material, then characterise and compare the defect types and densities produced by each irradiation type.

2 – Methods

2.1 – Material

A simple model alloy of Fe9Cr was studied for this work. Ferritic-martensitic steels containing ~9at%Cr are prime candidates for use as structural steels in future generation fission and fusion power plants [45]. Model alloys are simpler for studying fundamental behaviours of the material characteristics that remain relevant for the more complex variants. Studying this simple alloy will enable subtle radiation differences in the microstructure to be identified that are much more difficult to observe in commercial steels (particularly nanostructured steels like T91 or ODS steels).

A one hundred pound (~45 kg) heat of the Fe9%Cr alloy was melted at the Paul D. Merica Research Laboratory in New York, and provided in the form of a 10mm extruded bar. The bar was rolled to ~3mm thick, and then annealed in an argon atmosphere at 950°C for 15 min and at 750°C for 1 hour (with air cooling after each anneal). This resulted in the ferritic grain structure shown in Figure 1(a) with a low dislocation density of ~6×10^{12} /m^2, as shown in Figure 1(b). The same alloy was also studied by Bachhav et al. [37], Bhattacharyya et al. [46], and Haley et al. [47], and also the same alloy heat prior to the annealing treatment by Gelles et al. [48]. In atomic-percent, the composition of the alloy is 9.36% Cr, 0.05% Ni, 0.02% V, and 0.01% each of C, Si, P and Mn (see APT study by Bachhav et al. [37]).

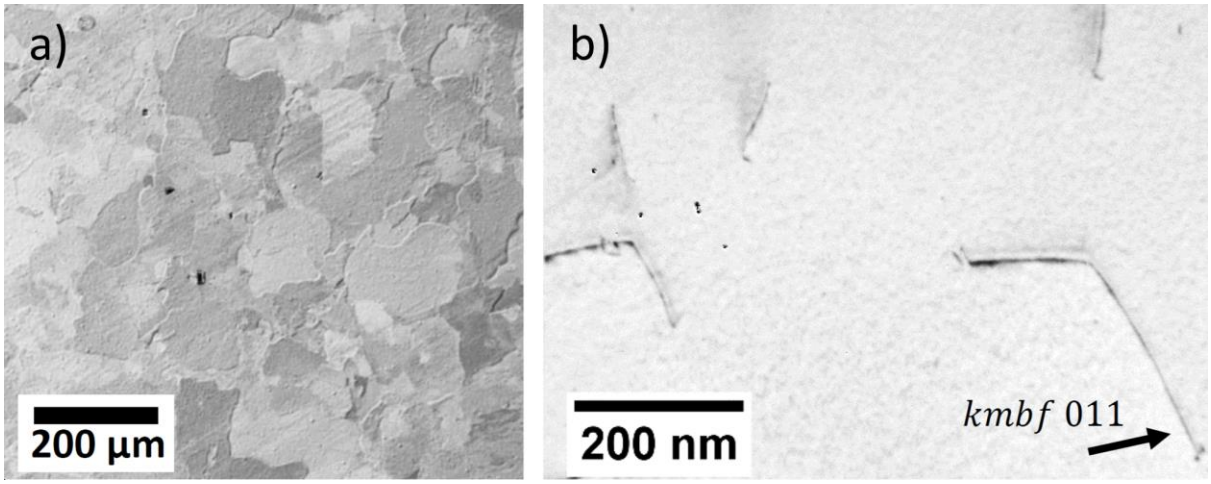

Figure 1: a) Secondary Electron SEM image of the ferritic grain structure in the Fe9Cr model alloy, and b) TEM kinematical bright field (kmbf) image of a typical region of unirradiated FIB-prepared Fe9Cr. The dislocation density is approximately 6×10^{12} /m^2.

2.2 – Irradiation experiments

Neutron irradiation was conducted at the Advanced Test Reactor (ATR) at Idaho National Laboratory. The irradiation temperature was 315-335°C, and the neutron fluence after 202 days was 1.2×10^{25} n/m^2 (E>1MeV) [49,50]. This corresponds to a dose of 1.6 displacements per atom (dpa) at a rate of 9.4×10^{-8} dpa/s, as calculated using FISPACT-2 with the TENDL-2014 neutron cross-section library [51] and SPECTER-modelled [52] ATR neutron-fluence spectrum [49]. The amount of transmutation gas was predicted to be low (~0.4 He-appm and 7.3 H-appm). Analysis of the microstructure of this neutron-irradiated alloy has already been conducted for a separate paper [47].

Charged particle irradiations were conducted to match the neutron irradiation temperature and NRT-dpa dose as closely as possible. Both the self-ion and proton irradiation experiments were conducted at slightly lower temperatures of 290°C and 300°C, respectively, due to later improvements to the thermal analysis of the neutron-irradiation experiment (the neutron irradiation experiment initially indicated a temperature of 290°C). Self-ion irradiation was conducted at the Surrey Ion Beam Centre using 2MeV Fe^+ ions to a fluence of 1.9×10^{19} ions/m^2 over 48 hours. This amounts to a dose of 2.2 dpa in the Bragg peak, and a rate of 1×10^{-5} dpa/s. Proton irradiation was

conducted at the Dalton Cumbria Facility using 1.2MeV protons to a fluence of 2.8×10^{23} protons/m^2 over 49 hours. This amounts to a dose of ~40 dpa in the Bragg peak (at ~9µm depth), but the area studied for this comparison resides 2.0-2.5µm into the profile. In this region, the dose is on average 1.9 dpa, with a dose rate of 1×10^{-5} dpa/s. The displacement energy used for all dpa calculations was 40eV. Table 1 summarises these experimental conditions. Figure 2 shows the dpa and the injected-ion profiles for self-ion and proton irradiations.

	Neutrons	Protons	Self-ions
Dose (dpa)	1.6	1.9 (2.0-2.5µm)	2.2 (peak)
Dose rate (dpa/s)	9×10^{-8}	1×10^{-5}	1×10^{-5}
Irradiation time (days)	202	2	2
Temperature (°C)	315-335	302	290
Fluence (/m²)	1.2×10^{25} (>1MeV)	2.8×10^{23}	1.9×10^{19}
Energy (MeV)	ATR mixed spectrum	1.2	2.0

Table 1: Irradiation parameters for the neutron, proton, and self-ion irradiation experiments.

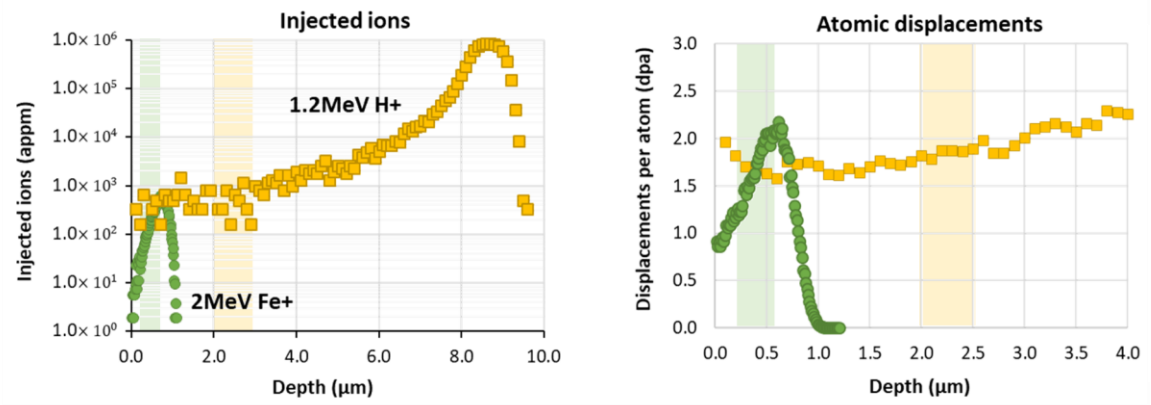

Figure 2: Injected ions and displacements per atom as a function of depth for the 2MeV self-ion irradiation and 1.2MeV proton irradiation. The parts of the dose-profiles that were characterised are indicated by the shaded areas.

2.3 – On the use of SRIM for calculating dpa

Calculations of dpa by SRIM [43] for proton irradiation can be inconsistent for different calculation methods, as noted by Stoller [42]. We find this to be particularly true for proton irradiation. Charged particle implantations in this study were simulated using SRIM, and then, following the recommendations of Stoller et al. [42], the damage energy (the kinetic energy available for creating atomic displacements [53]) was calculated, and subsequently the dpa via the NRT

equation [44]. Stoller et al. [42] explain the process for calculating the NRT damage energy as either the sum of the SRIM "phonons", or the beam energy minus energy dissipated via ionisation. The latter of these is the more physical definition of the damage energy, since the actual phonons produced by a recoil atom do not cause displacements [32].

The beam energy, B, is the average energy of an implanted ion over a given range in the damage profile. Integrated over the depth of the damage profile, this is simply the initial ion energy that was input into SRIM (otherwise it will have the more generic units of eV/Å·ion). In the SRIM model, the beam energy B is the sum of the beam energy lost to the target atom T_{Beam} ("Energy from ions" in e2recoil.txt), the beam energy deposited via ionisation I_{Beam}("Ioniz. By ions" in ioniz.txt), and the beam energy deposited as phonons P_{Beam} ("Phonons by ion" in phonon.txt).

$$B = T_{Beam} + I_{Beam} + P_{Beam} \quad (1)$$

The damage energy D is then,

$$D = B - (I_{Beam} + I_{Atoms}) \quad (2)$$

$$D = P_{Beam} + P_{Atoms} \quad (3)$$

where I_{Atoms} and P_{Atoms} are the energies lost by the recoiling atoms via ionisation and phonon production respectively. The vacancies can then be calculated by the NRT equation [44],

$$N_{Vac} = 0.8 \times \frac{D}{2E_D} \quad (4)$$

The factor of 0.8 is an efficiency term estimated by Norgett et al. [44] to reflect the number of defects that remain at the end of a cascade (when the thermal spike has completely cooled and recovered). Though this has become the standard measure of dpa, the actual number of surviving

defects at the end of a cascade is highly variable depending on the energy of the cascade, the material, the temperature, and the defects present before the cascade [32,54–56].

The damage profile for a 2MeV iron-ion into iron is shown in Figure 3. We have included in the plot calculations from the vacancy output of SRIM, and the vacancies as calculated from equation (4) via equations (2) and via (3). The vacancy profile prediction by SRIM is nearly equal for all three calculations. Inconsistencies are evident when we consider proton irradiation. Figure 3 also shows the damage profile for a 1.2MeV proton into iron, but we see that each calculation produces a different value. This indicates how SRIM can be less reliable for light-ion damage calculations.

For this work, we used the dpa as calculated via the standard NRT method, where the damage energy was calculated by deducting ionisation losses from the beam energy. Figure 3 highlights a major cause for uncertainty in SRIM-predictions of the NRT-dpa for light-ion irradiations.

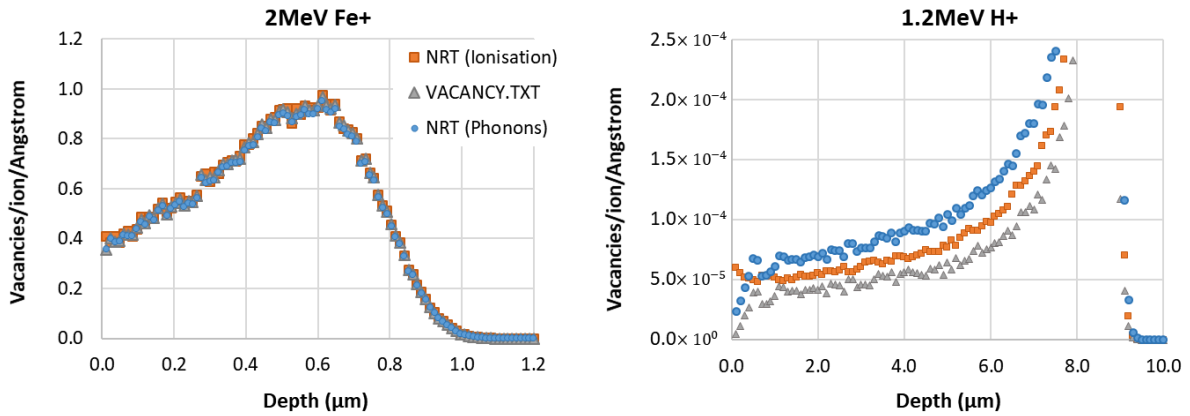

Figure 3: SRIM-produced vacancy production rates as a function of depth, using the vacancy.txt SRIM output, and the NRT methods. NRT (Ionisation) indicates the damage energy was calculated by deducting the ionisation losses from the beam energy; and NRT (Phonons) indicates the damage energy was calculated by summing the phonon SRIM outputs.

2.4 – TEM analysis methods

Samples were prepared for transmission electron microscopy (TEM) via the Focussed Ion Beam (FIB) lift-out method [57]. Jet-electropolishing was not used since the volume of material available was too small. To remove 30kV Ga+ FIB damage, a final thinning from ~180nm foil

thickness to ~100nm was conducted using 2kV Ga+ ions. Precession weak-beam dark field was used to image the dislocation loops, following the technique described by Haley et al. [47], using a JEOL 2100 microscope operating at 200kV with a LaB_6 source and scripted beam control. Dislocation loop and void measurements were conducted using the standard techniques described by Jenkins and Kirk [58]. Foil thickness, for measuring densities by volume, was measured via the convergent beam electron diffraction (CBED) method [59].

Electron Energy Loss Spectroscopy (EELS) in scanning-TEM (STEM) mode was conducted on a JEOL ARM200F operating at 200kV with a cold-FEG source, and equipped with a Quantum Gatan Imaging Filter (GIF). Convergence and collection half angles were 31.5mrad and 41.0mrad respectively. EELS spectrum images were captured with a 0.25eV energy resolution over 2048 channels between 400 and 912eV to capture oxygen K, chromium L and iron L edges. Hyperspy [60] was used to remove X-ray energy spikes from the data, and then denoising was conducted using the principal component analysis (PCA) method [61]. The energy spectra were then fitted using the Hartree-Slater model and the elemental intensities were extracted from the corresponding edges. The foils used for EELS were too thin to use CBED to determine their thickness; instead, the log-ratio method [62,63] was used (which is also more convenient than CBED when conducting EELS measurements).

3 – Results

Micrographs of the neutron, proton and self-ion irradiated microstructures are shown in Figure 4 (a)-(f). Both the neutron-irradiated and proton irradiated Fe9Cr contain a very heterogeneous distribution of dislocation loops, with the vast majority of the visible damage lying close to low angle grain boundaries or dislocations. In contrast, the microstructure of the self-ion irradiated alloys within the shallow damage depth is mostly homogeneous and has a higher visible density of damage features.

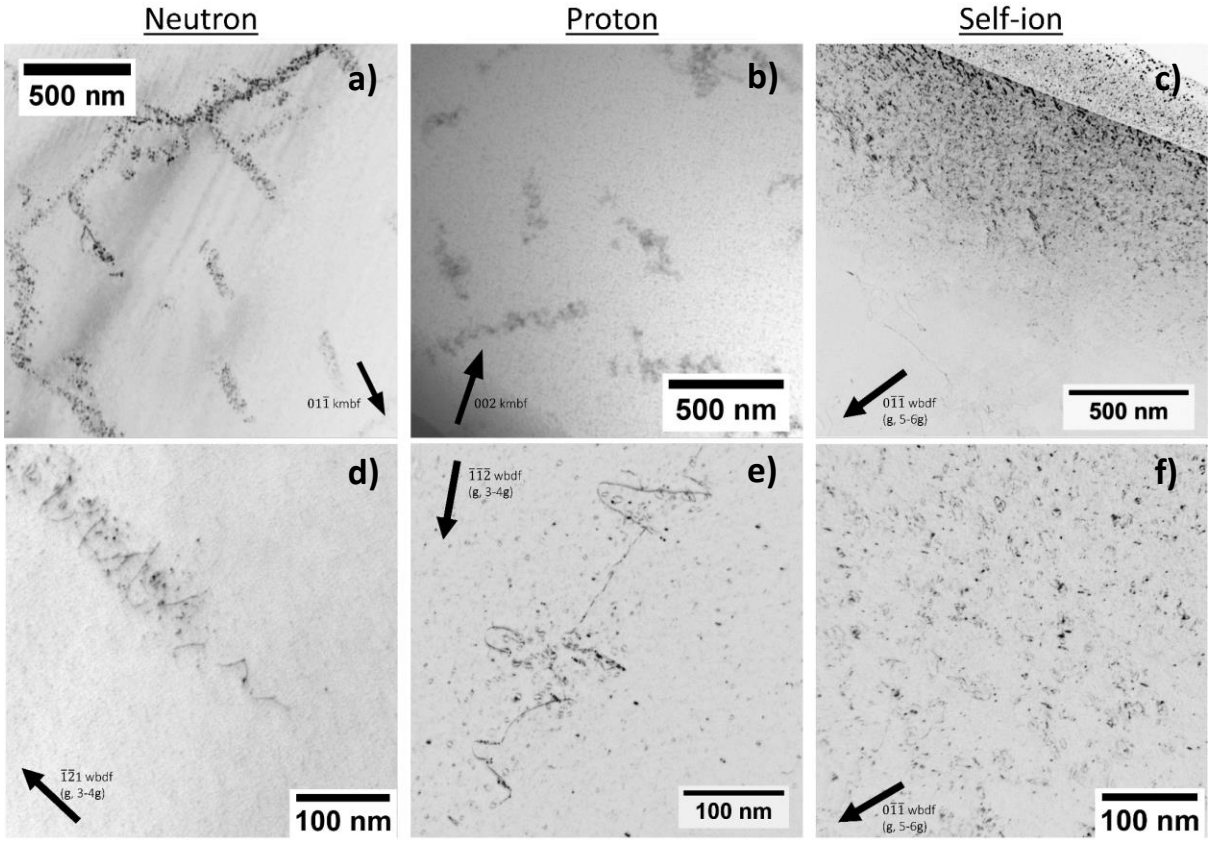

Figure 4: Typical micrographs showing the microstructures of neutron, proton and self-ion irradiated Fe9Cr. The proton damage was captured 2.0-2.5μm from the surface, and the higher magnification image of the self-ion damage was captured ~200-500nm from the surface.

The neutron and proton irradiated alloys contain a large number of helical dislocations, around which defects are clustered. The self-ion irradiated sample does not contain dislocations as distinctly helical as those in the neutron or proton irradiated material, though some do have the "zig-zag" appearance typical of helical dislocations (see supplementary material SM-1).

For each irradiation condition, the dislocation loops were characterised for their number-density, Burgers vectors and sizes. The interstitial or vacancy nature of the dislocation loops was also determined via the inside-outside method, and cavities were investigated using the under/over focus method. EELS was used to characterise the redistribution of alloyed chromium.

3.1 – Burgers vectors and number densities of dislocation loops

The Burgers vectors of the dislocation loops present in each of the neutron, proton and self-ion irradiated alloys were determined by capturing micrographs using various g-vector conditions, and observing the change in visibility of the dislocation loops. An example of simple **g**.**b** analysis is shown in Figure 5 for the self-ion irradiated alloy. To determine the overall dislocation loop densities and the fraction of $\langle 111 \rangle$ and $\langle 100 \rangle$-type loops present, statistical analysis was used, following the method described by Prokhodtseva et al. [64]. A minimum size of 2nm was assigned for counting the defects in order to eliminate possible errors in counting the smallest features due to their similarities with surface oxide and FIB-damage.

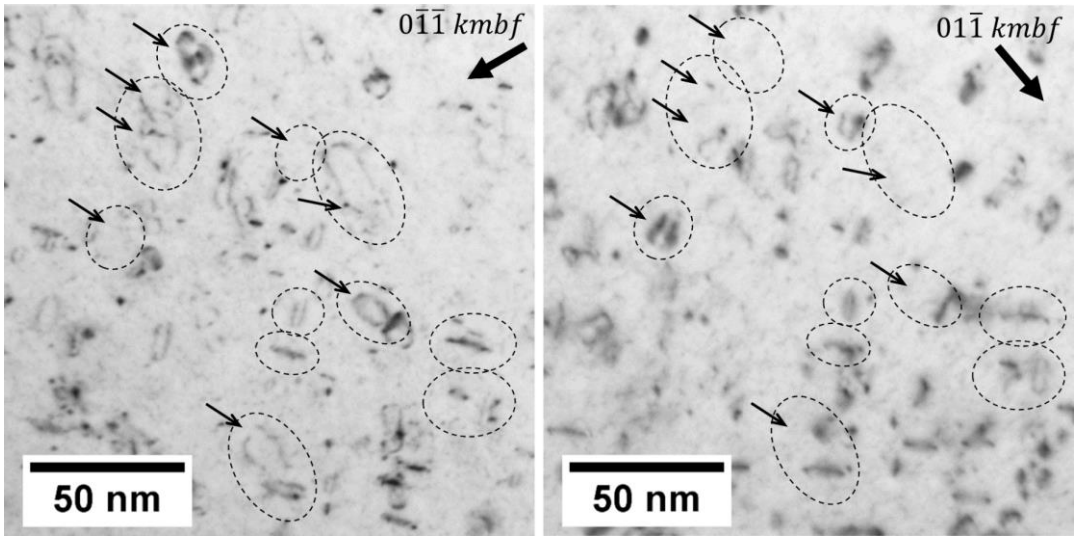

Figure 5: Example of simple Burgers vector analysis of dislocation loops in the self-ion irradiated Fe9Cr. Defects visible in both kinematical two-beam bright-field conditions, with ***g****=*$0\bar{1}\bar{1}$ *and* $01\bar{1}$*, must be* $\langle 100 \rangle$*-type loops, whereas those unique to each condition are* $\langle 111 \rangle$*-type.*

The visible loop density for each imaging condition and for each irradiation is shown in SM-2. A summary of the total loop density according to the statistical analysis for each irradiation is shown in Figure 6, and the Burgers vectors in Figure 7. In the case of the proton-irradiated material, dislocation loops were counted both in an area of high loop density (close to helical dislocations) and in an area of low loop density (far from dislocations or boundaries). For the neutron-irradiated material, the number of visible loops in areas of low loop density was too few for an accurate statistical analysis; in the areas between helical dislocation structures and the low-angle sub-grain boundaries, the microstructure was absent of loops distinguishable from oxide or FIB damage for

hundreds of nanometres. An area sized 680x320nm was considered typical of the low loop density regions, in which only one clear loop larger than 2nm was visible. This suggests a number density in this region on the order of $2\pm1 \times10^{20}$ loops/m^3.

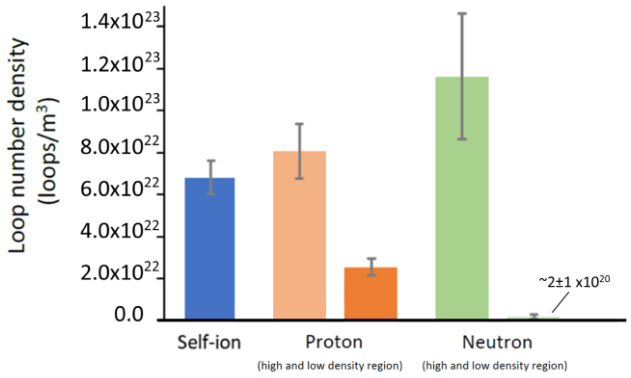

Figure 6: Dislocation loop volume number densities in self-ion, proton, and neutron irradiated Fe9Cr. High density loop counts were taken from volumes within helical dislocations, whereas counts from low density regions were taken from volumes far from dislocations or grain boundaries.

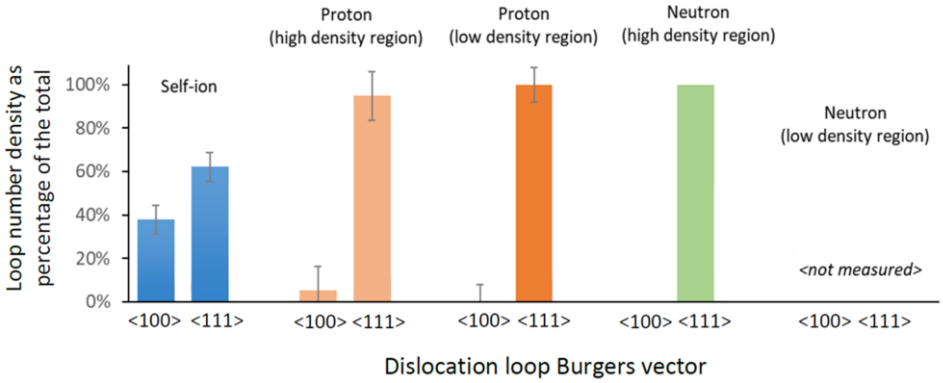

Figure 7: Burgers vectors of dislocation loops in self-ion, proton, and neutron irradiated Fe9Cr. High density loop counts were taken from volumes within helical dislocations, whereas counts from low density regions were taken from volumes far from dislocations or grain boundaries.

Figure 6 shows that the number densities of the dislocation loops in the neutron and proton irradiated microstructures are very heterogeneous (as is also clear from the micrographs in Figure 4). The difference between high and low-density regions in the neutron irradiated material is most extreme, with a very high loop density concentrated with the helical dislocations (~$1x10^{23}$ /m^3); while very few loops are visible in the low-density regions (~$2x10^{20}$ /m^3).

The proton-irradiated microstructure has a much greater number of visible loops in the low-density regions than in similar regions in the neutron-irradiated microstructure ($2.5x10^{21}$/m^3 and

$2x10^{20}/m^3$ respectively). The high-density loop counts in the proton-irradiated material, like the neutron, were taken from a region around a helical dislocation, but were measured to have a slightly lower density (~$8x10^{22}$ $/m^3$) than the neutron irradiated material.

The self-ion irradiated microstructure contains loops more homogeneously distributed. While some clustering of defects was visible, there was no clear high-density and low-density regions. Since the damage layer of the self-ion irradiation was very shallow (~600nm), we did not make an accurate measurement of the variance in loop density due to the damage profile. However, we note that from the micrographs, such a correlation with the damage profile (calculated with SRIM) is not visually apparent.

The microstructures of the proton and neutron-irradiated Fe9Cr are dominated by ⟨111⟩-type loops; the self-ion irradiated Fe9Cr contained a mix of ⟨100⟩- and ⟨111⟩-type loops.

3.2 – The nature of dislocation loops

The interstitial or vacancy nature of the dislocation loops was measured by the inside-outside method [59]. The results of this analysis on the neutron-irradiated material is shown in reference [47]. In Figure 8, a selection of dislocation loops from a high density region of the proton-irradiated Fe9Cr is shown, which inside-outside contrast suggests are interstitial-type. This is as expected based on previous work [65–67], and agrees well with the findings of interstitial loops in the neutron irradiated Fe9Cr alloy [47].

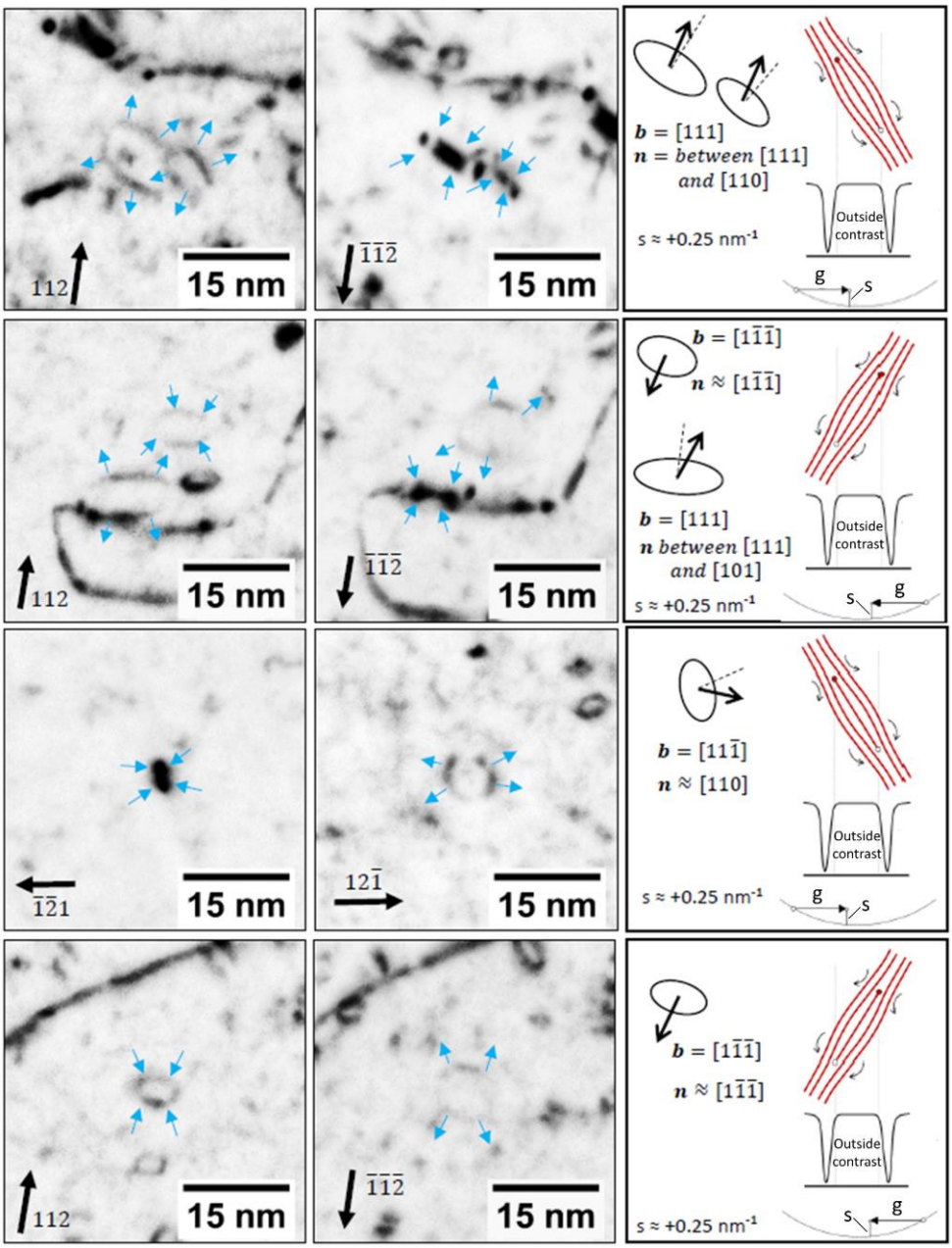

Figure 8: Inside-outside contrast analysis of dislocation loops in the proton-irradiated Fe9Cr. All loops analysed this way displayed contrast typical of interstitial-type loops.

Figure 9 shows the same analysis for the self-ion irradiated Fe9Cr; we also show here details of the tilt series used to identify the sense of the habit plane of the indicated loops. A unit cell is included in Figure 9 to aid in interpreting the sample orientation and inclination of the defects. Surprisingly, the inside-outside contrast is the opposite to that of similar defects in the neutron- and proton- irradiated Fe9Cr. This analysis therefore suggests these loops are vacancy-type. Furthermore, no interstitial loops were found (of the 30 analysed). This is highly unusual based on

prior studies of dislocation loops in ferritic materials [65–68]; the implications of this finding are discussed in section 4.

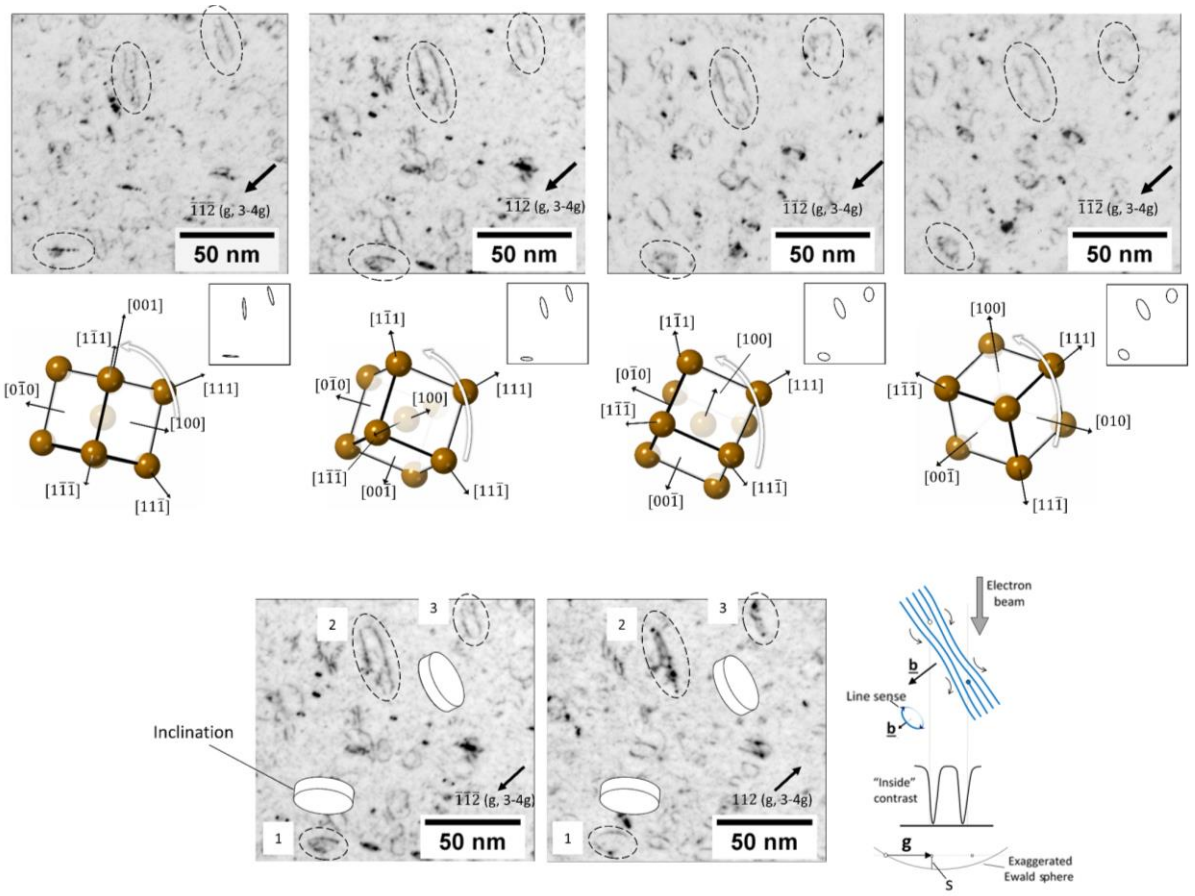

Figure 9: Tilt series and inside-outside contrast analysis of dislocation loops in the self-ion irradiated Fe9Cr,analysed at depths from 250nm up to 580nm from the surface. All loops analysed this way displayed contrast typical of vacancy-type loops.

3.3 – Size of dislocation loops

An accurate measurement of each dislocation loop's size was determined by averaging the major diameter of each loop as seen in both plus- and minus- g weak-beam conditions, in order to rule out inside-outside contrast effects on the apparent size (see Figure 8, for example). The measurements for each irradiation are presented as histograms in Figure 10, with the mean dislocation loop size (>2nm) also indicated.

These results show that the dislocation loops in the self-ion irradiated Fe9Cr had a mean diameter ~2nm larger than those in the neutron and proton-irradiated materials, and a larger size variance. The dislocation loops within helical-dislocations for the proton and neutron-irradiated Fe9Cr were similar. Since very few defects were seen in regions far from grain boundaries and helical dislocations in the neutron irradiated Fe9Cr, it was not possible to accurately measure the size distribution in these regions. For the proton-irradiated Fe9Cr, many more loops easily distinguishable from FIB damage were seen, and so a meaningful size distribution could be measured.

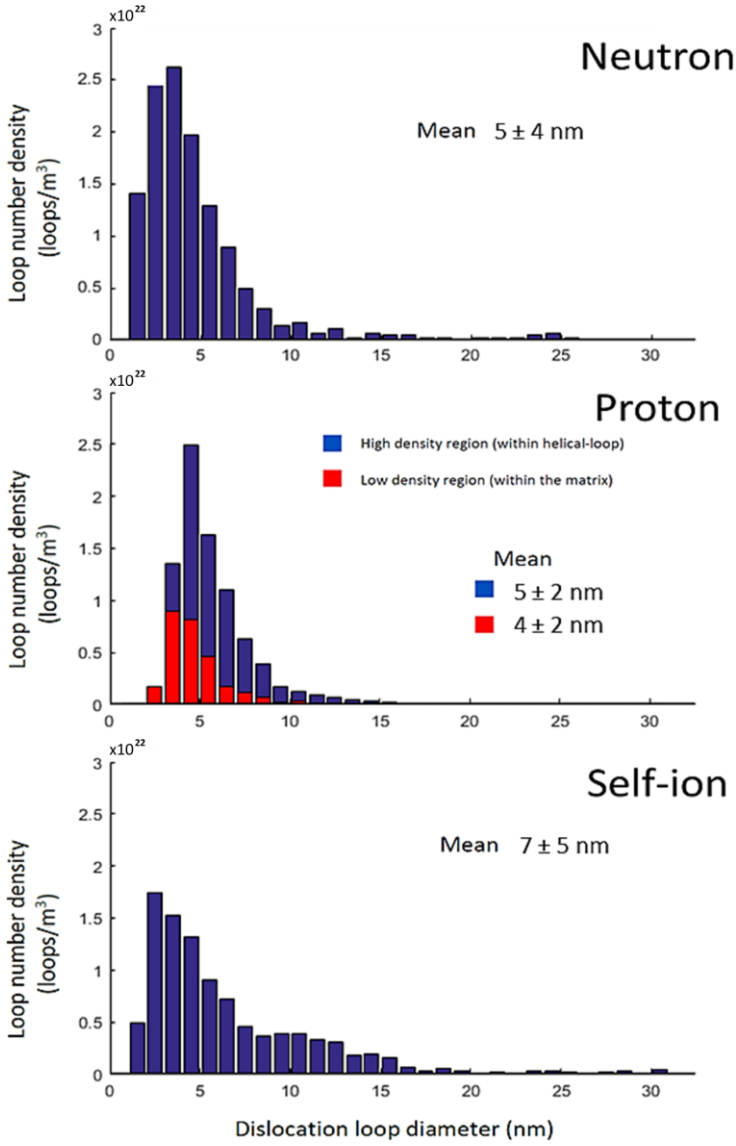

Figure 10: Dislocation loop size distributions for each irradiation. The mean size is indicated for each, where the error is the standard deviation.

3.4 – Cavities

The under-over focus technique was used to capture micrographs of voids in the neutron, self-ion and proton-irradiated Fe9Cr. A selection of these are shown in Figure 11; arrows in the negative-focus micrographs of Figure 11 indicate a selection of void-like features that were identified. Diffraction contrast was removed from the images by subtracting the positive focus condition from the negative focus.

The neutron-irradiated alloy was found to contain very small (<2nm) features with contrast typical of voids. The self-ion irradiated sample contained similar features that were barely distinguishable from the background fluctuations, and so it is difficult to say with any confidence that any of these features are voids, rather than simply surface oxide or contaminants. The contrast of such defects is difficult to interpret, since small particles, such as surface oxide or any other small contaminants on the surface of the TEM foil, can show the same contrast [59]. However, given that mostly vacancy dislocation loops were found in the self-ion irradiated alloy, it is reasonable to expect the cavity population to be very low.

Micrographs of the proton-irradiated sample are shown in Figure 11 at two different magnifications. A rich density of void-like features is clearly visible at both magnifications with much stronger contrast than those seen in the neutron and self-ion irradiated samples. Considering the bright contrast, and the varied spatial and size distribution, we are much more confident in designating these features as cavities than for those in the self-ion irradiated alloys.

Table 2 summarises measurements of these cavities from various points in the microstructure; on the straight dislocation segments, inside helical segments, close to the straight segments, and far from the dislocation. Cavities were sized following the criteria set by Ruehle and Wilkens [69]. We have also provided measurements of the features in the neutron and self-ion irradiated material. It

is important to note the uncertainty that the features in the self-ion irradiated sample are definitely voids.

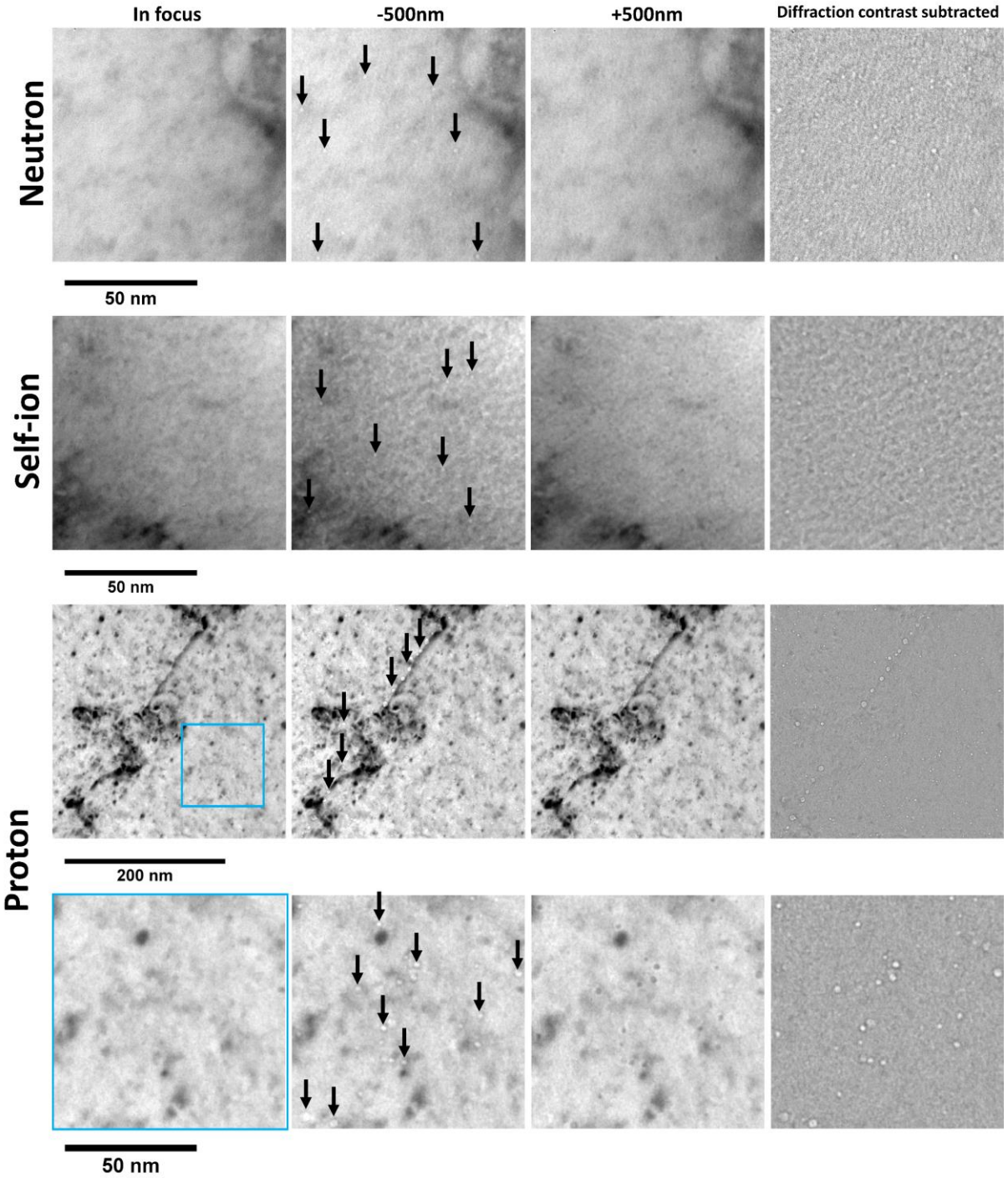

395 *Figure 11: Under-over focus images of the neutron, self-ion and proton irradiated Fe9Cr, showing nano-cavities in each. The contrast of the void-like defects in the self-ion irradiated is very poor, and may in fact be simply surface oxide on the foil or contamination.*

	Neutron Within helix	**Neutron** Outside helix	**Self-ion**	**Proton** Within helical segment	**Proton** On dislocation line	**Proton** Close to straight dislocation	**Proton** Far from dislocation
Number density (voids/m³)	1.7±0.6 x10^{22} (2±2 x10^{21})	8.2±1.2 x10^{22} (none)	2.2±0.6 x10^{22} (9±4 x10^{21})	2.4±0.6 x10^{22} (1.3±0.4 x10^{22})	8±2** (all)	2.3±0.6 x10^{22} (1±1 x10^{21})	5.7±0.9 x10^{22} (2.2±0.6 x10^{21})
Mean diameter (nm)	1.2±0.4	1.5±0.3	1.9±0.4	2.4±1.2	4.5±1.1	1.7±0.3	2.0±0.6
Maximum diameter (nm)	2.2	1.6	2.6	5.4	6.5	2.4	3.5
Minimum diameter (nm)	0.8	0.8	1.2	1.1	3.3	1.1	1.1
Number counted	10	30	14	19	12	16	39

** units of voids/100nm
Parentheses indicate voids >2nm. Size distributions can be found in SM3.

Table 2: Summary of measurements made from void-like defects shown in Figure 11. There is considerable uncertainty in designating the features in the self-ion irradiated sample as voids due to poor contrast and similarity to foil surface contamination/oxide.

The out-of-focus features in the neutron and self-ion irradiated sample were mostly <2nm and spherical. The larger cavities in the proton irradiated Fe9Cr were facetted, as shown in Figure 12.

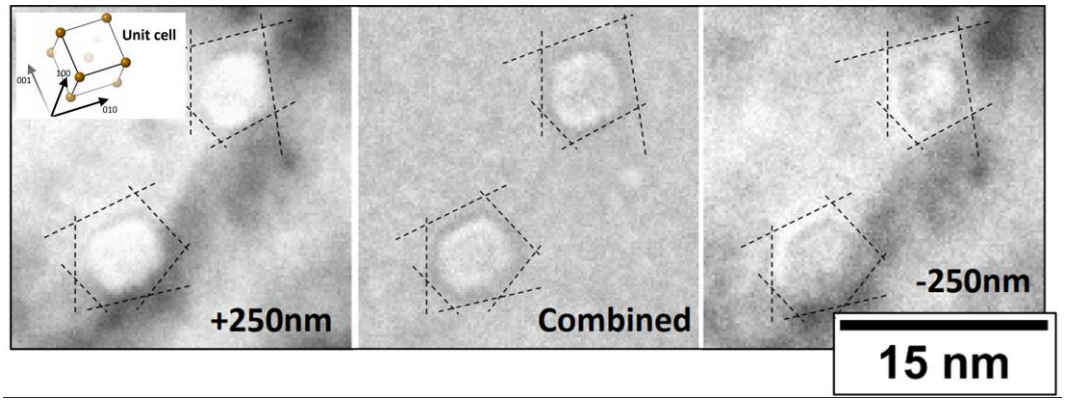

Figure 12: Under-over focus images of proton irradiated Fe9Cr, showing facetted cavities, with orientation of the unit cell indicated.

3.4 – Chromium precipitation

Chromium-rich phases were investigated using EELS in foils typically 20-30nm thick. Figure 13 shows quantitative chromium maps extracted from the EELS spectra from each irradiated Fe9Cr alloy. Chromium clusters are visible in the neutron and proton-irradiated alloys, but not in the self-

ion irradiated alloy. We did not see any oxygen associated with these clusters, which rules out the possibility these are chromium-oxide.

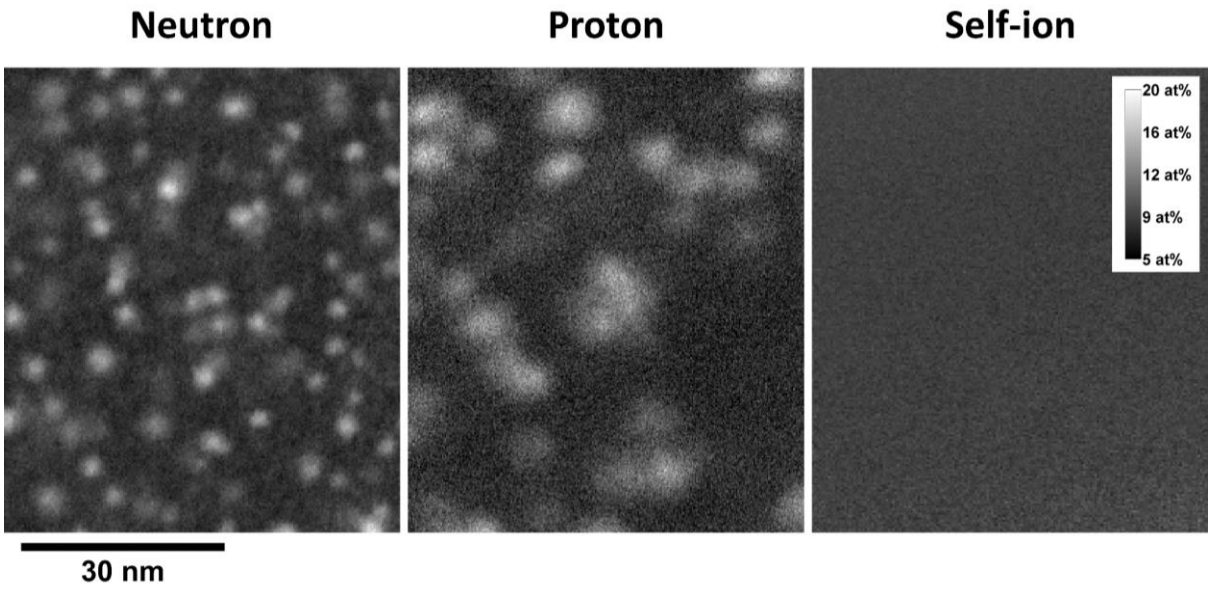

Figure 13: Quantitative EELS chromium maps from the neutron, proton and self-ion irradiated (depth ~300nm, ~1.3 dpa) Fe9Cr. Solute chromium redistributed into nanoclusters for the neutron and proton irradiated Fe9Cr, but not in the self-ion irradiated.

The maps represent the average chromium composition through the foil at each pixel. The composition measured over a precipitate therefore does not equate to the composition of the precipitate itself since it includes the material above and below it in the 2D image projection. A simple method to subtract the background contributions to the signal is via a "hard sphere approximation". This is where we treat the cluster as a uniform sphere with a uniform composition, C, throughout the structure. Knowing the composition of the FeCr matrix M, the composition of a hard sphere of diameter D within a foil of thickness T can be determined via Equation 5.

$$A = C\left(\frac{D}{T}\right) + M\left(\frac{T-D}{T}\right) \quad (5)$$

Where A is the composition measured from the 2D EELS map at the centre of the cluster. This can be easily rearrange to give the cluster composition C.

An issue with this approach for chromium clusters such as these is that the edge of these clusters is not well defined. This means a different definition of the size of the cluster will change the relative contributions of cluster and matrix to the average composition measured in the map, and this will affect the determined composition of the cluster. To circumvent this issue, we applied a "Gaussian-distribution approximation". We assumed that the distribution of chromium around the centre of the cluster follows a Gaussian distribution that is symmetrical in 3D. This allows us to fit a simple Gaussian function to the 2D map of a cluster. Using the standard deviation, σ, of the fitted function, the distribution of chromium through the foil thickness, t, can be then estimated knowing that the centre of the cluster in a 2D composition map is the mean composition of the column through the foil. The quantitative chromium distribution can then be normalised to this mean composition over the foil thickness (known from the low-loss EELS spectrum), with the background matrix contribution also known from parts of the map absent of precipitate. This can be summarised by Equation 6. A description of this approach, with diagrams to facilitate understanding the steps involved, is included in SM-4.

(6)

$$I(z) = I_{BG} + \frac{A - I_{BG}}{\frac{1}{N}\sum_{z=-t/2}^{z=t/2} \exp(-\frac{z^2}{2\sigma^2})} \exp(-\frac{z^2}{2\sigma^2})$$

In equation 6, I is the chromium content as a function of depth z, I_{BG} is the matrix composition (term M in equation 5), A is the composition measured from the 2D EELS map through the centre of the cluster, σ is the standard deviation of the distribution, and N is the number of terms in the summation. Two additional assumptions are necessary; the cluster is contained entirely within the foil, and only one cluster is within the column of foil (i.e. not two or more stacked on top of each other). The breakdown of this latter assumption can lead to overestimated core composition values, which could exceed 100at%.

Table 3 summarises the results of this analysis, including number density and volume fraction calculations. We have quoted the cluster size as 2σ and included the amplitude of the function; this should allow the composition to be easily recalculated for comparison to other studies that define clusters differently. With the diameter defined this way, the size corresponds to the diameter of a spherical volume containing ~68% of the chromium signal associated with the precipitate (assuming the Gaussian distribution holds true).

	Neutron	**Proton**
Number density (clusters/m^3)	7.4 ± 0.4 x10^{23}	2.5±0.3 x10^{23}
Mean diameter (nm)	2.1±0.4	4.4±1.0
Mean composition (at%)	41±20	*25.2±6.8* *
Peak composition (at%)	57±22	31±9
Matrix composition (at%)	8.0±0.6	7.9±1.2
Volume Fraction	0.0013±0.0008	0.0041±0.0028
Number counted	67	51

* subsequent imaging at higher magnification and down a zone axis reveal a better defined structure of the precipitates, and indicate a higher mean composition of ~68at%Cr, Figure 14.

Table 3: Summary of the measurements of chromium clusters in the neutron and proton irradiated Fe9Cr

The width of the electron beam used to acquire the EELS maps can have an impact on both the size and composition of small particles. For the chromium map of the proton irradiated Fe9Cr, the clusters have a diameter approximately twice that of those in the neutron irradiated sample, and a composition that is much lower than is typically observed for α'-phases. To investigate the morphology of these clusters with better precision, we acquired additional EELS maps at higher magnification and with a much finer (and more stable) electron beam.

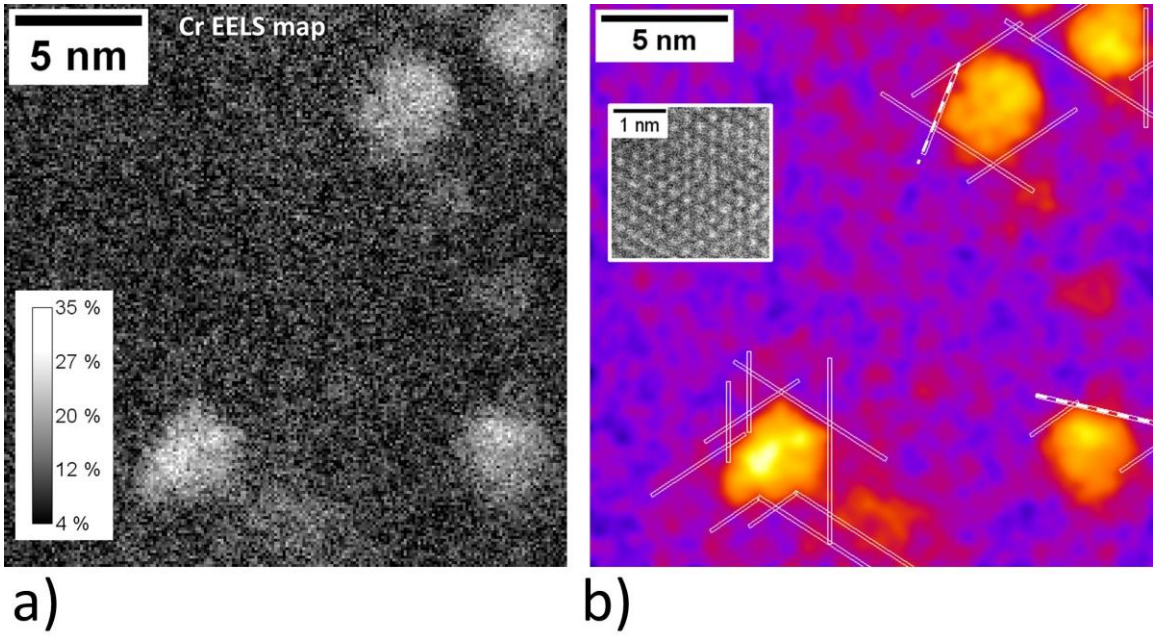

Figure 14: High magnification EELS maps showing chromium in proton irradiated Fe9Cr; a) is a quantitative chromium map, and b) depicts the same data qualitatively with simple image filtering applied (digitally scaled by 3, and Gaussian filtered with σ=6 pixels), shown with a coloured look-up table ("Fire" in ImageJ [70]). Subfigure in b) shows Z-contrast atomic columns to indicate [111] crystal orientation.

Figure 14(a) shows a chromium map captured down a [111] zone axis. From the Z-contrast STEM images also acquired, the atomic lattice could be easily resolved, and without deviation from focus over the course of the scan. Figure 15 shows subsequent analysis that indicates the chromium distribution through the structure is not Gaussian like those in the images in Figure 13. Instead, the distribution follows a semi-circle distribution, implying these clusters have a chromium profile that is constant for at least some of its volume.

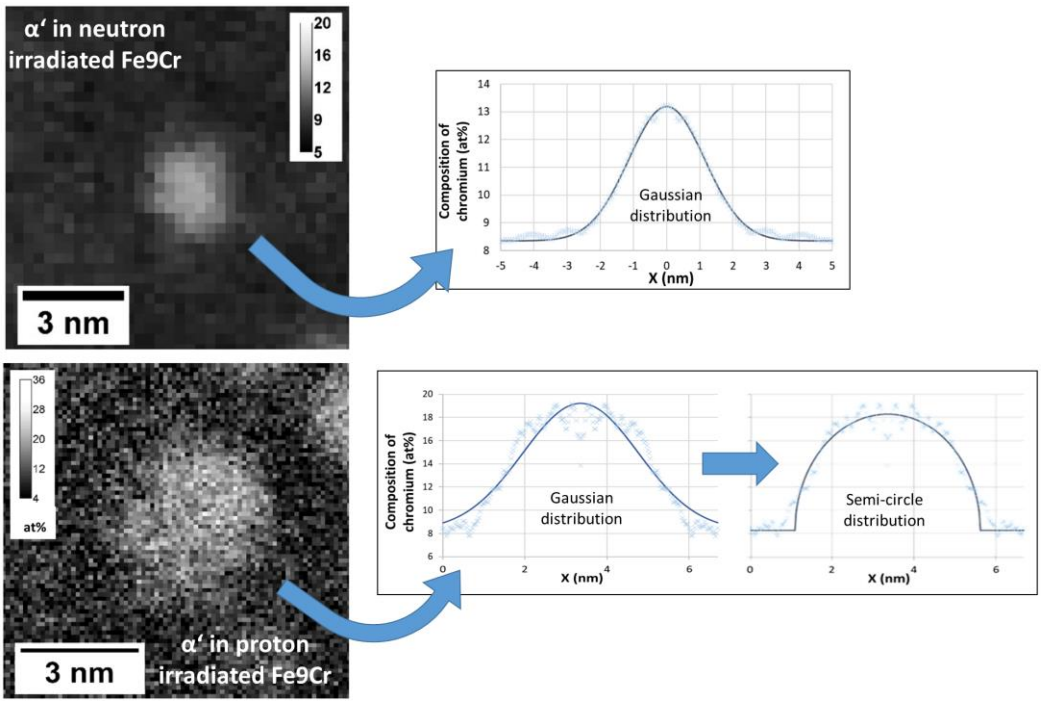

Figure 15: Example chromium clusters and their corresponding radial profiles. Examples of the distribution function used to fit the profiles are shown.

Applying a hard-sphere approximation to the profiles in the higher magnification EELS map, we find the composition of these clusters to be 68±10 at% (n=4), and mean diameter 4.0±0.4 nm. This suggests the analysis of the clusters in Table 3 of the proton irradiated Fe9Cr underestimates the cluster composition, but the size and number density are in good agreement.

Figure 14(b) was produced by applying a Gaussian filter to the chromium map (σ radius = 6 pixels, as applied to a map digitally scaled by a factor of 3), and is shown with a coloured lookup table ("Fire" in ImageJ [70]). This shows the clusters have facets, from the flat edges seen aligned mostly with $\langle 111 \rangle$ directions (facets drawn with bold dashed white lines are aligned closer to $\langle 312 \rangle$). If we assume these facets are orthogonal to the view direction, then this would suggest they are facetted mostly on $\{110\}$ planes, though not all edges seem facetted.

4 – Discussion

The microstructures of Fe9Cr after neutron irradiation, proton and self-ion irradiation differ significantly from each other. Differences were observed in the dislocation loop population and homogeneity, the sizes of the loops, the Burgers vector of the loops, the nature of the loops, the void population and sizes, and the formation of chromium α'-phases. These results, and the mechanisms that could be responsible, are discussed here.

4.1 – On the formation of dislocation loops

The neutron-irradiated Fe9Cr, (studied in [47]) contained large areas (several hundred nanometres) with a very low number density of visible dislocation loops (as low as ~10^{20} loops/m^3), with the majority of the visible damage clustered around dislocations and low-angle grain boundaries. Considering the dislocation density, this indicates the high loop-density regions occupy ~3% of the volume. This observation is consistent with similar observations of neutron damage in FeCr by Hernandez-Mayoral et al. [7]. From the work of Bhattacharyya [46], we note that the same alloy irradiated by neutrons to the same dose, at the same temperature, but ~3.3x faster, contained a more homogeneous distribution of dislocation loops which suggests the influence of dose rate on final microstructure is significant for even relatively small changes in flux.

Dislocation loops were also observed in the self-ion and proton irradiated Fe9Cr, but the matrix (far from grain boundary or dislocation sinks) of both contained a much greater population of visible dislocation loops. This indicates that these faster dose-rate experiments result in enhanced loop growth and retention than is the case for the slower neutron irradiation – an effect of dose rate that is also supported by the self-ion dose-rate experiments by Xu [8].

The proton-irradiated microstructure replicated the heterogeneous spatial distribution of the dislocation loops found after neutron irradiation fairly well, with similar helical dislocations and loop

clustering observed (although no sub-grain boundaries were seen for comparison). Also, like the neutron-irradiated alloy, mostly ⟨111⟩-type dislocation loops were seen.

Many dislocations in the proton-irradiated Fe9Cr appeared as uniform helices, though some in the material appeared as straight dislocations with occasional helical segments (such as the one shown in Figure 3). This suggests that the mechanism for dislocation climb into helical dislocations during irradiation can be disrupted. This might be that vacancy defects could uncouple from the dislocation, leaving behind cavities; or that the initial vacancy-climb process described by Haley et al. [47] is being affected somehow. We should note that not all lift-outs contained these straight/helical segmented dislocations.

The self-ion irradiated microstructure is very different to the neutron- and proton- irradiated microstructures. Although some loops were clustered together, the damage was much more homogeneous throughout the first 600nm depth of the foil, after which the loop population declined with depth. The loops in the self-ion irradiated Fe9Cr were much larger (mean size 7±5 nm) than those even in the high-density regions of the neutron- (5±4 nm) and proton- (5±2 nm) irradiated Fe9Cr.

The self-ion irradiated Fe9Cr also contained a high fraction of ⟨100⟩ loops (~40%). The ⟨100⟩ type loops are typically immobile [71], and are produced either by loop-loop coalescence [71,72] or via rotation of the loop habit plane while it is small [73], or both. The ⟨100⟩ type loops are more stable at higher temperatures [34], with the loop Burgers vectors transitioning from majority ⟨111⟩ to majority ⟨100⟩ between 300˚C and 400˚C [35]. The observation of a greater number of ⟨100⟩ loops for a constant temperature usually suggests that ⟨111⟩ defects (produced in-cascades) were more mobile [74,75], as it implies ⟨100⟩ loop production via the 111-mechanism [72] occurs more frequently. This suggests that the loops produced during self-ion irradiation may have been more mobile than loops produced during neutron irradiation, despite the neutron irradiation being the

hotter experiment. Cascade overlap has been observed to accelerate the formation of ⟨100⟩ loops [55]. Due to the large cascades produced by 2 MeV self-ion irradiation, cascade overlap is more significant than from proton irradiation. At high dose rates (self-ion irradiation), a lower fraction of the interstitials and vacancies produced in cascades recombine (before a subsequent overlapping cascade) than at low dose rates (neutron irradiation). Thus, the significant cascade overlap of the 2 MeV self-ion irradiation could be expected to accelerate the formation of ⟨100⟩-type dislocation loops.

In the self-ion irradiated Fe9Cr, the loops were vacancy in nature, whereas those in the neutron and proton-irradiated Fe9Cr were interstitial. Vacancy loops are rarely reported in ferritic materials, with most irradiation studies (heavy-ion and neutron) reporting interstitial-type [65–68]. Vacancy loops only tend to appear in situations where there is a large interstitial sink close by (e.g. the foil surface) [76,77]. Interstitials exhibit a much larger strain field on the matrix than vacancies, and thus migrate easily and "see" other interstitials more easily than vacancies [1]. Interstitial clusters therefore should coarsen more quickly than vacancy clusters, leading to the majority of visible dislocation loops being interstitial. Therefore, the most likely explanation for the observation of vacancy loops here is that interstitials are being lost to some sink.

The only interstitial sink visible from the micrographs is the surface of the sample. Surface effects on defects can extend up to 200-300nm in iron-based materials [78], and so interstitial losses are an important consideration when working with thin foils or shallow damage profiles. Our measurements of loop nature in the ion-irradiated sample were conducted at depths up to 580nm from the surface, i.e. deeper than depths at which surface effects are considered significant.

If interstitials were being lost to the sample surface during irradiation, this would leave a supersaturation of vacancies in the matrix, which could then cluster as dislocation loops. This would suggest the interstitial defects are able to migrate hundreds of nanometres to reach the surface

during irradiation. The temperature spikes of high-energy cascades and the displacement of impurity atoms might enable this. Large and frequent cascades might also suppress the segregation of alloying elements and substitutional impurities that can reduce a dislocation loop's mobility [79,80], thus extending their glide range.

Vacancy clusters usually favour a 3D void structure over 2D dislocation loops in iron [81], with dislocation loops the less stable defect for clusters smaller than ~50. Though Gilbert et al.'s modelling [81] of this result does not consider the effect of chromium on this stability, it is surprising that so many large vacancy loops exist in this Fe9Cr alloy. Gilbert et al.'s work would suggest that a large fraction of the vacancy clusters here were produced in cascades in large enough clusters (30-50 vacancies) for dislocation loop formation. However, Molecular Dynamics (MD) suggests this does not happen frequently; Soneda et al. [82] simulated 50keV cascades in iron and saw only one vacancy loop produced after 100 simulated cascades. The collapse of a cascade into a vacancy-rich core is rare in iron [56], since cascades mostly split into sub-cascades for PKA energies above only a few keV [83]. Most interstitials produced by a high energy cascade are contained within glissile ($\langle 111 \rangle$ dislocation loops) [84] and/or sessile (e.g. C15) clusters [85]; a lower fraction of the vacancies cluster together, with most remaining as point defects [82,84]. However, Sand et al.'s MD simulations show a significant increase in the formation of vacancy dislocation loops in iron when cascades overlap with pre-existing vacancy clusters (2 cases in 40 simulations of cascades overlapping with a dense vacancy cluster). If there is a large amount of interstitial loss to the surface, in addition to cascade overlap playing a significant role in vacancy-loop production during self-ion irradiation of this Fe9Cr alloy, then a vacancy-loop dominated microstructure might be expected.

The precise mechanisms for our observation of vacancy loops is unclear at the moment, though preliminary findings of the loop nature in other alloys irradiated in the same experiment and separate experiments indicate this is not an isolated result. This is an ongoing investigation.

4.2 – On the formation of cavities

The cavity population densities and sizes in the proton-irradiated Fe9Cr were substantially greater than those seen in the neutron and self-ion irradiated alloys. Those in the proton-irradiated sample were ~5nm in diameter on average, whereas the self-ion and neutron-irradiated samples contained mostly <2nm voids.

Voids are rarely seen in self-ion irradiated microstructures at ~1 dpa doses [35,67], but this may be in part due to the difficulty in distinguishing small voids from surface oxide or any other surface contaminant, or small particle. Although many examples of defects with void-like contrast were visible in the self-ion irradiated Fe9Cr, they all had very poor contrast compared to similar-sized features in the proton-irradiated Fe9Cr, so these might actually be surface contaminants. If these features are voids, then their visible density is low. This would normally indicate that the vacancy defects mostly exist as clusters too small to identify from surface oxide and/or contaminants; however, a substantial population of the dislocation loops in the self-ion irradiated Fe9Cr are vacancy type, which may explain why no larger voids are visible from the under-over focus technique.

A large population of large cavities exists in the proton-irradiated Fe9Cr (up to 7nm), which suggests that proton irradiation enhances void growth. Implanted hydrogen is often not considered to be influential during proton irradiation [16,86], since the majority of the hydrogen is deposited beyond the Bragg peak, several microns from where measurements are conducted. Furthermore, hydrogen is highly mobile in iron at these temperatures, and so would usually be expected to quickly escape the material [86]. However, as shown in Figure 2, the implanted hydrogen at shallow depths of the proton-irradiated alloys is between 500 and 1000appm. Considering that hydrogen is easily trapped at defects like vacancy clusters [87], it is quite possible that some hydrogen remains in the microstructure long enough to affect the vacancy-defects. Any molecular hydrogen present in

vacancy clusters would need to dissociate for it to escape the cluster [87,88], and so it could be trapped for much longer. It was not possible to make a distinction between void and bubble in this study. The small cavities in the neutron irradiated Fe9Cr may also contain hydrogen, and also helium, which originate from transmutation reactions (~0.4 He-appm and 7.3 H-appm). As with the proton, we were unable to distinguish void from bubble; however, at these concentrations, we would not expect them to be bubbles [89]. For the proton irradiated sample, some of the cavities were facetted. This has been argued previously as a means to distinguish void from gas bubble [1], since the pressure of a bubble might be expected to force the cavity to take a spherical shape; however, experimental observations [89] and computer simulations [90] show this is not necessarily the case.

Some cavities in the proton-irradiated Fe9Cr were seen in chains on top of screw dislocations. Like the neutron-irradiated alloy [47], many helical dislocations were found in the proton-irradiated Fe9Cr, but some examples in the proton irradiated material comprised straight and helical segments. The helical segments are absent of these cavity-chains, which would support previous analysis [47] that these helical dislocations are produced by vacancy-mediated climb, rather than interstitial. Hence, vacancies were removed from the local microstructure by the dislocation, so cavities did not form. It is not clear why cavity-chains formed in some places, and helical dislocations formed in others. It could be an indication that the irradiation temperature is very close to the temperature at which it is preferable for vacancies to cluster as a cavity, rather than on the dislocation. The dislocations would therefore contain a mixture of cavity-chains and helical segments. There would still be a flux of vacancies towards the dislocation (due to the vacancy-bias), which could lead to void nucleation close to the dislocation core. Alternatively, it is possible that vacancies uncoupled from the helical dislocation and formed voids, though it is unclear whether such a transformation would be favourable, or even why such cavity-chains were not seen in the apparently hotter neutron irradiated Fe9Cr. Though the temperature of the proton irradiation appeared fairly stable

640 throughout, occasional spikes in current are known to have occurred. The resultant temperature spike will have been too quick to detect, but could affect the microstructure nonetheless.

4.3 – On the redistribution of chromium

Electron energy-loss spectroscopy was used to determine whether, in response to neutron, proton or self-ion irradiation, α' phase chromium precipitates formed. Chromium-rich precipitates
645 were found in the neutron- and proton- irradiated Fe9Cr; no such precipitation or segregation was identified in the self-ion irradiated Fe9Cr. The lack of observed chromium precipitation or even segregation to dislocation loops in the self-ion irradiated Fe9Cr is another reason why dislocation loops might be more mobile (as discussed previously in section 4.1).

The analysis of chromium clusters in the neutron and proton-irradiated Fe9Cr indicates that
650 the core composition of the clusters exceed 50at% chromium in both cases, which is typical of α'-phases [37,91]. However, there is not a well-defined threshold composition of chromium that defines when a cluster is α'-phase, rather than simply a cluster; and there is inconsistency in the literature over how a cluster is defined, with various isosurfaces used to threshold clustered regions in Atom Probe Tomography (APT) data. This makes it difficult to reliably compare the chromium
655 compositions measured from different experiments and measurement techniques.

The measurements of the core composition in the Cr-rich regions in the neutron and proton-irradiated Fe9Cr are similar to the APT measurements by Kuksenko et al. [91] on similar FeCr alloys neutron-irradiated to a lower dose (Fe9Cr and Fe12Cr irradiated with neutrons to 0.6dpa at 300°C, each containing α'-phases with core compositions of 55.1at% and 58.5at% respectively). This
660 supports our designation of these clusters as α'-phases. They are unlikely to be simply dislocation loops with chromium segregation due to their consistently spherical or facetted geometry, rather than any resemblance to a loop viewed side-on or elliptical, and aligned with crystallographic axes. Kuksenko et al. [91] and Bachhav et al. [92] also saw nickel, silicon and phosphorus associated with

such chromium clusters (via APT). We were unable to detect any such clustering via EELS in our materials.

The chromium precipitates' number density in the proton-irradiated Fe9Cr was three times smaller than in the neutron-irradiated alloy. The precipitates were first measured as having an average composition of ~20at% Cr, whereas the neutron-irradiated precipitates had an average composition of ~40at%. The composition measurements of the clusters in the proton-irradiated sample in Table 3 were shown to underestimate the composition of chromium, since subsequent imaging at higher magnification and down a zone axis (Figure 14) revealed a better defined structure of the precipitates (as far as showing facets), and indicated a higher mean composition of ~68at%Cr. We were unable to capture higher magnification EELS maps from the neutron-irradiated sample.

The neutron-irradiated Fe9Cr alloy studied here is from the same batch of materials (and same irradiation campaign) as the Fe9Cr alloy studied by Bachhav et al. [37] and Bhattacharyya [46] In their case, the alloy was irradiated at the same temperature and to a similar dose (1.5 dpa), but at a dose-rate roughly 3-4 -times faster. The population of α' precipitates measured here in the neutron-irradiated Fe9Cr alloy ($7.4\pm0.4 \times 10^{23}$ m^{-3}) is nearly an order of magnitude higher than that which Bachhav et al. (APT) and Bhattacharyya et al. (energy-filtered TEM) recorded (8.5×10^{22} m^{-3} and 5.5×10^{22} m^{-3} respectively). This cannot be attributed to the ~0.2 dpa difference in dose, or uncertainties in the temperature, and so must be due to the difference in dose rate.

We can also rule out differences in measurement technique as a cause for the differences. Energy filtered TEM (EFTEM) measurements have a higher threshold for the detection of small clusters than EELS with PCA filtering, so it is understandable that EFTEM measurements by Bhattacharyya et al. should underestimate the number of chromium clusters. Aberrations in APT due to evaporation rate differences between matrix and α'-phase can be significant for clusters ~1nm in radius [93]; this limits the resolution of APT. However, unless the chromium distribution is non-

uniform, we would expect the APT measurements by Bachhav et al. to account for the majority of clusters in the material. We can therefore be certain that this small dose-rate difference has been significant for these alloys. This could be due to the large difference in the length of irradiations (202 days versus 55 days [49]). This means the neutron irradiated alloy studied here was thermally aged for longer, and so there is a longer time between overlapping cascades for diffusion processes to occur.

The population density of precipitates in the proton-irradiated alloy was ~3× that measured by Bachhav et al. in neutron-irradiated material [37]. Accelerated chromium precipitation can only be attributed to accelerated diffusion of chromium during irradiation [37,91,94]. Proton irradiation appears to enhance defect mobility in relation to void and loop growth, and so it is reasonable to expect chromium diffusion to also be enhanced. This would be expected from the increased fraction of freely-migrating defects produced by proton-induced cascades over neutron or self-ion irradiation [1,16].

The accelerated diffusion of interstitials and vacancies during irradiation leads to the redistribution of the matrix atoms over time, which can cause a local concentration of chromium to exceed the solubility limit [37,91,94–96], and cause a new α' phase clusters to form. These will then continue to grow and become further enriched. Since no such precipitation was seen in the self-ion irradiated Fe9Cr, the large cascades, the injected iron-atoms, or both, could be suppressing this process [40,97,98].

A very large cascade could disrupt a local concentration of chromium that may otherwise become α'. Frequent bombardment of the lattice by such large cascades would mean this process occurs often [40,98]. Therefore, α' precipitates would struggle to nucleate due to this ballistic mixing. Large cascades from protons are rarer, which may allow time for a chromium cluster to coarsen and become further enriched, leading to the observed microstructure.

Tissot et al. [97] showed that injected interstitials from 2MeV Fe+ irradiation can suppress the formation of α' in Fe15Cr, and argued that this proves ballistic dissolution does not occur. We argue this only proves injected material also suppresses α' formation, and does not eliminate ballistic dissolution as occurring at all. Ballistic dissolution is shown to be important for dose rate effects from the phase-field modelling by Ke et al. [98], and Kinetic Monte Carlo simulations by Soisson et al. [40]. A 15Cr alloy is much more susceptible to α' formation than the 9Cr alloy studied here (which has a composition very close to the solubility limit of chromium [37,91]). From the lack of any chromium separation seen in this study from 2MeV Fe+ irradiation (conducted at a similar dose rate to Tissot et al.), ballistic dissolution cannot be ruled out as a cause for α' suppression during heavy-ion irradiation (in addition to possible injected-interstitial effects).

Ballistic dissolution was found by Soisson et al. [40] to be more significant if the material contains a high density of point defect sinks, since the population of freely migrating defects (which enhance diffusion) will be reduced. This is particularly important for heavy-ion irradiated materials since most defects are created as clusters (dislocation loops) in-cascade [32].

5 – Conclusions

TEM was used to study an alloy of Fe9Cr irradiated with neutrons, self-ions or protons to a dose of ~2dpa and at temperatures close to 300°C. Self-ion and proton irradiation are undoubtedly useful techniques that allow fast screening of how a material will behave in a fission or fusion environment, or for improving our understanding of how radiation damage accumulates in a material. Our observations of the microstructure of Fe9Cr after neutron, proton or self-ion irradiation highlight the need for careful use of surrogate particle irradiation by showing previously unreported microstructural differences that may occur. This is particularly important with respect to the interstitial/vacancy loop types, the effects of injected hydrogen, the spatial distribution of defects, and changes to the chemistry. The key findings are listed below.

1- Irradiation to a similar dose and at a similar temperature by self-ions and by protons produces damage that is inconsistent with the neutron damage observations. The dislocation loops in self-ion irradiated Fe9Cr were homogeneously distributed, and larger (~7nm in diameter) than those in the neutron and proton-irradiated alloys (~5nm in both). The dislocation loops in the self-ion irradiated alloy were mostly vacancy-type, whereas those in the neutron and proton-irradiated samples were all interstitial. Vacancy loops have not been previously reported on this scale in bulk implanted iron-based materials. Voids, mostly <2nm in size, were identified in the self-ion irradiated Fe9Cr, but these were not clear and possibly only surface oxide. The dislocation loops in the proton-irradiated samples were heterogeneously distributed through the foil, similar to the neutron-irradiated alloy, with higher loop densities close to helical-shaped dislocations.

2- Proton irradiation of Fe9Cr produced a large population of cavities (~$4x10^{22}$ /m^3) throughout the microstructure. Larger voids ~5nm in diameter were also found aligned in chains alongside or through screw dislocations. The line dislocations comprised straight sections (with the cavity-chains) and helical segments, containing fewer and smaller cavities ~2nm in size. The helical segments, like helical dislocations seen in the neutron irradiated Fe9Cr, were produced by a vacancy-biased defect flux. Since the voids in the self-ion and neutron irradiated Fe9Cr were much smaller (~2nm) and less confidently designated as voids, the large population of cavities in the proton-irradiated alloy may be evidence that injected hydrogen is stabilising void growth.

3- The matrix of neutron- and proton irradiated Fe9Cr contained a rich density of chromium clusters ($7.4x10^{23}$ m^{-3} and $2.5x10^{23}$ m^{-3} in the neutron- and proton- irradiated alloys respectively), which were identified as α'-phases. No such precipitates were found in the self-ion irradiated sample. The dose-rate of the proton and self-ion irradiation experiments were similar, which suggests that injected interstitials and/or large cascades of the self-ion irradiation were disrupting early stage chromium clusters, which may otherwise have gone on to form α' phases.

4- The density of chromium clusters in neutron irradiated Fe9Cr was ~10x higher than the density of clusters reported by Bachhav et al. [37] in the same alloy irradiated with neutrons at a 3.3x faster dose-rate. The dose-rate effect is therefore significant for only a factor of 3-4 difference for neutron irradiation, possibly due to the ballistic dissolution of newly formed chromium clusters at higher dose-rates.

Acknowledgments

STEM and EELS measurements were performed using 'South of England Analytical Electron Microscope' at the University of Oxford, supported by a UK Engineering and Physical Sciences Research Council (EPSRC) grant EP/K040375/1. This work was also supported by the Fusion Centre for Doctoral Training (EP/L01663X/1), and Platform Grant 'Advanced Nuclear Materials' (EP/P001645/1). The authors also acknowledge the US DOE National Scientific Users Facility Program sponsored UCSB ATR-1 irradiation, and FIB access at the Centre for Advanced Energy Studies (CAES) which was supported by the U.S. Department of Energy, Office of Nuclear Energy under DOE Idaho Operations Office Contrast DE-AC07-051D14517 as part of a Nuclear Science User Facilities experiment. Parts of this work were conducted at the Materials Research Facility (UKAEA), supported by equipment funded by National Nuclear Users Facility and the Henry Royce Institute (EP/P021727/1). The UK National Ion Beam Centre supported irradiation experiments at the Dalton Cumbria Facility and Surrey Ion Beam Centre.

References

[1] G.S. Was, Fundamentals of Radiation Materials Science, Springer, 2007. doi:10.1007/978-3-540-49472-0.

[2] S. Ishino, N. Sekimura, Role of charged particle irradiations in the study of radiation damage correlation, J. Nucl. Mater. 174 (1990) 158–167. doi:10.1016/0022-3115(90)90230-K.

[3] D.J. Mazey, Fundamental aspects of high-energy ion-beam simulation techniques and their relevance to fusion materials studies, J. Nucl. Mater. 174 (1990) 196–209. doi:10.1016/0022-3115(90)90234-E.

[4] T. Okita, T. Sato, N. Sekimura, F.A. Garner, L.R. Greenwood, The primary origin of dose rate effects on microstructural evolution of austenitic alloys during neutron irradiation, J. Nucl. Mater. 307–311 (2002) 322–326. doi:10.1016/S0022-3115(02)01202-3.

[5] L.K. Mansur, Correlation of neutron and heavy-ion damage. II. The predicted temperature shift if swelling with changes in radiation dose rate, J. Nucl. Mater. 78 (1978) 156–160. doi:10.1016/0022-3115(78)90514-7.
[6] C.D. Hardie, C.A. Williams, S. Xu, S.G. Roberts, Effects of irradiation temperature and dose rate on the mechanical properties of self-ion implanted Fe and Fe-Cr alloys, J. Nucl. Mater. 439 (2013) 33–40. doi:10.1016/j.jnucmat.2013.03.052.
[7] M. Hernández-Mayoral, C. Heintze, E. Oñorbe, Transmission electron microscopy investigation of the microstructure of Fe–Cr alloys induced by neutron and ion irradiation at 300 °C, J. Nucl. Mater. 474 (2016) 88–98. doi:10.1016/j.jnucmat.2016.03.002.
[8] S. Xu, A Study of Irradiation Damage in Iron and Fe-Cr Alloys, Univ. Oxford DPhil Thesis. (2013). https://ora.ox.ac.uk/objects/uuid:fec4b2d0-411e-4c20-862d-e5fd884367f3.
[9] C.D. Hardie, S.G. Roberts, Nanoindentation of model Fe–Cr alloys with self-ion irradiation, J. Nucl. Mater. 433 (2013) 174–179. doi:10.1016/j.jnucmat.2012.09.003.
[10] F.M. Halliday, D.E.J. Armstrong, J.D. Murphy, S.G. Roberts, Nanoindentation and Micromechanical Testing of Iron-Chromium Alloys Implanted with Iron Ions, Adv. Mater. Res. 59 (2008) 304–307. doi:10.4028/www.scientific.net/AMR.59.304.
[11] C.D. Hardie, G.R. Odette, Y. Wu, S. Akhmadaliev, S.G. Roberts, Mechanical properties and plasticity size effect of Fe-6%Cr irradiated by Fe ions and by neutrons, J. Nucl. Mater. 482 (2016) 236–247. doi:10.1016/j.jnucmat.2016.10.028.
[12] A. Reichardt, M. Ionescu, J. Davis, L. Edwards, R.P. Harrison, P. Hosemann, D. Bhattacharyya, In situ micro tensile testing of He+2 ion irradiated and implanted single crystal nickel film, Acta Mater. 100 (2015) 147–154. doi:10.1016/J.ACTAMAT.2015.08.028.
[13] H.T. Vo, A. Reinhardt, D. Frazer, N. Bailey, P. Chou, P. Hosemann, In Situ Microtensile Testing for Ion Beam Irradiated Materials, in: Springer, Cham, 2019: pp. 593–603. doi:10.1007/978-3-030-04639-2_38.
[14] E.M. Grieveson, D.E.J. Armstrong, S. Xu, S.G. Roberts, Compression of self-ion implanted iron micropillars, J. Nucl. Mater. 430 (2012) 119–124. doi:10.1016/J.JNUCMAT.2012.06.014.
[15] C.A. Jones, A micromechanical investigation of proton irradiated oxide dispersion strengthened steels, Univ. Oxford DPhil Thesis. (2016). https://ora.ox.ac.uk/objects/uuid:fadd9abf-b5d0-4ea1-9d86-50628ec0476a.
[16] G.S. Was, J.T. Busby, T. Allen, E.A. Kenik, A. Jensson, S.M. Bruemmer, J. Gan, A.D. Edwards, P.M. Scott, P.L. Andreson, Emulation of neutron irradiation effects with protons: validation of principle, J. Nucl. Mater. 300 (2002) 198–216. doi:10.1016/S0022-3115(01)00751-6.
[17] M.J. Swenson, J.P. Wharry, The comparison of microstructure and nanocluster evolution in proton and neutron irradiated Fe–9%Cr ODS steel to 3 dpa at 500 °C, J. Nucl. Mater. 467 (2015) 97–112. doi:10.1016/J.JNUCMAT.2015.09.022.
[18] G. Gupta, Z. Jiao, A.N. Ham, J.T. Busby, G.S. Was, Microstructural evolution of proton irradiated T91, J. Nucl. Mater. 351 (2006) 162–173. doi:10.1016/j.jnucmat.2006.02.028.
[19] Z. Jiao, A.N. Ham, G.S. Was, Microstructure of helium-implanted and proton-irradiated T91 ferritic/martensitic steel, J. Nucl. Mater. 367–370 (2007) 440–445. doi:10.1016/J.JNUCMAT.2007.03.118.
[20] J.T. Busby, M.M. Sowa, G.S. Was, E.P. Simonen, Post-irradiation annealing of small defect clusters, Philos. Mag. 85 (2005) 609–617. doi:10.1080/02678370412331320071.
[21] M. Song, C.R. Lear, C.M. Parish, M. Wang, G.S. Was, Radiation tolerance of commercial and advanced alloys for core internals: a comprehensive microstructural characterization, J. Nucl. Mater. 510 (2018) 396–413. doi:10.1016/J.JNUCMAT.2018.08.035.
[22] K.J. Stephenson, G.S. Was, Comparison of the microstructure, deformation and crack initiation behavior of austenitic stainless steel irradiated in-reactor or with protons, J. Nucl. Mater. 456 (2015) 85–98. doi:10.1016/j.jnucmat.2014.08.021.
[23] Z.W. Zhang, C.T. Liu, X.L. Wang, M.K. Miller, D. Ma, G. Chen, J.R. Williams, B.A. Chin, Effects of proton irradiation on nanocluster precipitation in ferritic steel containing fcc alloying

additions, Acta Mater. 60 (2012) 3034–3046. doi:10.1016/J.ACTAMAT.2012.02.008.
[24] G.S. Was, M. Hash, R.G. Odette, Hardening and microstructure evolution in proton-irradiated model and commercial pressure-vessel steels, Philos. Mag. 85 (2005) 703–722. doi:10.1080/14786430412331319974.
[25] J.T. Busby, M.C. Hash, E.A. Kenik, G.S. Was, Precipitation of Second-Phase Particles in a Proton-Irradiated Model Alloy, Microsc. Microanal. 9 (2003) 604–605. doi:10.1017/S143192760344302X.
[26] Z. Jiao, G.S. Was, Segregation behavior in proton- and heavy-ion-irradiated ferritic–martensitic alloys, Acta Mater. 59 (2011) 4467–4481. doi:10.1016/j.actamat.2011.03.070.
[27] A. Reichardt, A. Lupinacci, D. Frazer, N. Bailey, H. Vo, C. Howard, Z. Jiao, A.M. Minor, P. Chou, P. Hosemann, Nanoindentation and in situ microcompression in different dose regimes of proton beam irradiated 304 SS, J. Nucl. Mater. 486 (2017) 323–331. doi:10.1016/J.JNUCMAT.2017.01.036.
[28] J. Gupta, J. Hure, B. Tanguy, L. Laffont, M.-C. Lafont, E. Andrieu, Characterization of ion irradiation effects on the microstructure, hardness, deformation and crack initiation behavior of austenitic stainless steel:Heavy ions vs protons, J. Nucl. Mater. 501 (2018) 45–58. doi:10.1016/J.JNUCMAT.2018.01.013.
[29] M. Wang, M. Song, C.R. Lear, G.S. Was, Irradiation assisted stress corrosion cracking of commercial and advanced alloys for light water reactor core internals, J. Nucl. Mater. 515 (2019) 52–70. doi:10.1016/J.JNUCMAT.2018.12.015.
[30] M.J. Swenson, J.P. Wharry, Nanocluster irradiation evolution in Fe-9%Cr ODS and ferritic-martensitic alloys, J. Nucl. Mater. 496 (2017) 24–40. doi:10.1016/j.jnucmat.2017.08.045.
[31] L. Malerba, Molecular dynamics simulation of displacement cascades in α-Fe: A critical review, J. Nucl. Mater. 351 (2006) 28–38. doi:10.1016/j.jnucmat.2006.02.023.
[32] R.E. Stoller, Role of cascade energy and temperature in primary defect formation in iron, J. Nucl. Mater. 276 (2000) 22–32. doi:10.1016/S0022-3115(99)00204-4.
[33] A. De Backer, A.E. Sand, K. Nordlund, L. Luneville, D. Simeone, S.L. Dudarev, Subcascade formation and defect cluster size scaling in high-energy collision events in metals, EPL (Europhysics Lett. 115 (2016) 26001. doi:10.1209/0295-5075/115/26001.
[34] S.L. Dudarev, R. Bullough, P.M. Derlet, Effect of the alpha-gamma Phase transition on the stability of dislocation loops in bcc iron, Phys. Rev. Lett. 100 (2008) 1–4. doi:10.1103/PhysRevLett.100.135503.
[35] Z. Yao, M.L. Jenkins, M. Hernández-Mayoral, M.A. Kirk, The temperature dependence of heavy-ion damage in iron: A microstructural transition at elevated temperatures, Philos. Mag. 90 (2010) 4623–4634. doi:10.1080/14786430903430981.
[36] L. Malerba, A. Caro, J. Wallenius, Multiscale modelling of radiation damage and phase transformations: The challenge of FeCr alloys, J. Nucl. Mater. 382 (2008) 112–125. doi:10.1016/j.jnucmat.2008.08.014.
[37] M. Bachhav, G. Robert Odette, E.A. Marquis, α' precipitation in neutron-irradiated Fe–Cr alloys, Scr. Mater. 74 (2014) 48–51. doi:10.1016/j.scriptamat.2013.10.001.
[38] M.J. Swenson, J.P. Wharry, TEM characterization of irradiated microstructure of Fe-9%Cr ODS and ferritic-martensitic alloys, J. Nucl. Mater. 502 (2018) 30–41. doi:10.1016/j.jnucmat.2018.01.062.
[39] G. Martin, Phase stability under irradiation: Ballistic effects, Phys. Rev. B. 30 (1984) 1424–1436. doi:10.1103/PhysRevB.30.1424.
[40] F. Soisson, E. Meslin, O. Tissot, Atomistic modeling of α' precipitation in Fe-Cr alloys under charged particles and neutron irradiations: Effects of ballistic mixing and sink densities, J. Nucl. Mater. 508 (2018) 583–594. doi:10.1016/J.JNUCMAT.2018.06.015.
[41] K. Nordlund, J. Wallenius, L. Malerba, Molecular dynamics simulations of threshold displacement energies in Fe, Nucl. Instruments Methods Phys. Res. Sect. B Beam Interact. with Mater. Atoms. 246 (2006) 322–332. doi:10.1016/J.NIMB.2006.01.003.

[42] R.E. Stoller, M.B. Toloczko, G.S. Was, A.G. Certain, S. Dwaraknath, F.A. Garner, On the use of SRIM for computing radiation damage exposure, Nucl. Instruments Methods Phys. Res. Sect. B Beam Interact. with Mater. Atoms. 310 (2013) 75–80. doi:10.1016/j.nimb.2013.05.008.
[43] J.F. Ziegler, M.D. Ziegler, J.P. Biersack, SRIM - The stopping and range of ions in matter (2010), Nucl. Instruments Methods Phys. Res. Sect. B Beam Interact. with Mater. Atoms. 268 (2010) 1818–1823. doi:10.1016/j.nimb.2010.02.091.
[44] M.J. Norgett, M.T. Robinson, I.M. Torrens, A proposed method of calculating displacement dose rates, Nucl. Eng. Des. 33 (1975) 50–54. doi:10.1016/0029-5493(75)90035-7.
[45] S.J. Zinkle, J.T. Busby, Structural materials for fission & fusion energy, Mater. Today. 12 (2009) 12–19. doi:10.1016/S1369-7021(09)70294-9.
[46] D. Bhattacharyya, T. Yamamoto, P. Wells, E. Marquis, M. Bachhav, Y. Wu, J. Davis, A. Xu, G.R. Odette, Microstructural changes and their effect on hardening in neutron irradiated Fe-Cr alloys, J. Nucl. Mater. 519 (2019) 274–286. doi:10.1016/j.jnucmat.2019.03.022.
[47] J.C. Haley, F. Liu, E. Tarleton, A.C.F. Cocks, G.R. Odette, S. Lozano-Perez, S.G. Roberts, Helical dislocations: Observation of vacancy defect bias of screw dislocations in neutron irradiated Fe–9Cr, Acta Mater. 181 (2019) 173–184. doi:10.1016/j.actamat.2019.09.031.
[48] D.S. Gelles, Microstructural examination of neutron-irradiated simple ferritic alloys, J. Nucl. Mater. 108–109 (1982) 515 26-515 26. doi:10.1016/0022-3115(82)90523-2.
[49] J.W. Nielsen, As-Run Physics Analysis for the UCSB--1 Experiment in the Advanced Test Reactor, Idaho Falls, ID (United States), 2015. doi:10.2172/1235196.
[50] As-Run Thermal Analysis for the UCSB-1 Experiment in the Advanced Test Reactor - Project No. 29607, Engineering Calculations and Analysis Report, Idaho National Laboratory, 2015.
[51] J.C. Sublet, J.W. Eastwood, J.G. Morgan, M.R. Gilbert, M. Fleming, W. Arter, FISPACT-II: An Advanced Simulation System for Activation, Transmutation and Material Modelling, Nucl. Data Sheets. 139 (2017) 77–137. doi:10.1016/J.NDS.2017.01.002.
[52] L.R. Greenwood, R.K. Smither, SPECTER: neutron damage calculations for materials irradiations, Argonne, IL, 1985. doi:10.2172/6022143.
[53] K. Nordlund, S.J. Zinkle, A.E. Sand, F. Granberg, R.S. Averback, R. Stoller, T. Suzudo, L. Malerba, F. Banhart, W.J. Weber, F. Willaime, S.L. Dudarev, D. Simeone, Improving atomic displacement and replacement calculations with physically realistic damage models, Nat. Commun. 9 (2018) 1084. doi:10.1038/s41467-018-03415-5.
[54] A.F. Calder, D.J. Bacon, A molecular dynamics study of displacement cascades in α-iron, J. Nucl. Mater. 207 (1993) 25–45. doi:10.1016/0022-3115(93)90245-T.
[55] J. Byggmästar, F. Granberg, A.E. Sand, A. Pirttikoski, R. Alexander, M.-C. Marinica, K. Nordlund, Collision cascades overlapping with self-interstitial defect clusters in Fe and W, J. Phys. Condens. Matter. 31 (2019) 245402. doi:10.1088/1361-648X/ab0682.
[56] A.E. Sand, J. Byggmästar, A. Zitting, K. Nordlund, Defect structures and statistics in overlapping cascade damage in fusion-relevant bcc metals, J. Nucl. Mater. 511 (2018) 64–74. doi:10.1016/J.JNUCMAT.2018.08.049.
[57] L.A. Giannuzzi, J.L. Drown, S.R. Brown, R.B. Irwin, F.A. Stevie, Applications of the FIB lift-out technique for TEM specimen preparation, Microsc. Res. Tech. 41 (1998) 285–290. doi:10.1002/(SICI)1097-0029(19980515)41:4<285::AID-JEMT1>3.0.CO;2-Q.
[58] M.L. Jenkins, M. Kirk, Characterization of Radiation Damage by Transmission Electron Microscopy, IOP Publishing Ltd, Bristol and Philadelphia, 2001. ISBN 0 7503 0748 X (hbk).
[59] D.B. Williams, C.B. Carter, Transmission Electron Microscopy: A Textbook for Materials Science, 2nd Edit., Springer, 2009. doi:10.1007/978-0-387-76501-3.
[60] F. de la Peña, T. Ostasevicius, V.T. Fauske, P. Burdet, E. Prestat, P. Jokubauskas, M. Nord, K.E. MacArthur, M. Sarahan, D.N. Johnstone, J. Taillon, A. Eljarrat, V. Migunov, J. Caron, T. Furnival, S. Mazzucco, T. Aarholt, M. Walls, T. Slater, F. Winkler, B. Martineau, G. Donval, R. McLeod, E.R. Hoglund, I. Alxneit, I. Hjorth, T. Henninen, L.F. Zagonel, A. Garmannslund, HyperSpy v1.4, (2018). doi:10.5281/ZENODO.1407391.

[61] M. Bosman, M. Watanabe, D.T.L. Alexander, V.J. Keast, Mapping chemical and bonding information using multivariate analysis of electron energy-loss spectrum images, Ultramicroscopy. 106 (2006) 1024–1032. doi:10.1016/J.ULTRAMIC.2006.04.016.
[62] T. Malis, S.C. Cheng, R.F. Egerton, EELS log-ratio technique for specimen-thickness measurement in the TEM, J. Electron Microsc. Tech. 8 (1988) 193–200. doi:10.1002/jemt.1060080206.
[63] D.R.G. Mitchell, Mean Free Path Estimator for Digital Micrograph, (2012). http://www.dmscripting.com/meanfreepathestimator.html (accessed September 3, 2018).
[64] A. Prokhodtseva, B. Décamps, A. Ramar, R. Schäublin, Impact of He and Cr on defect accumulation in ion-irradiated ultrahigh-purity Fe(Cr) alloys, Acta Mater. 61 (2013) 6958–6971. doi:10.1016/j.actamat.2013.08.007.
[65] S. Xu, Z. Yao, M.L. Jenkins, TEM characterisation of heavy-ion irradiation damage in FeCr alloys, J. Nucl. Mater. 386–388 (2009) 161–164. doi:10.1016/j.jnucmat.2008.12.078.
[66] I.M. Robertson, M.L. Jenkins, C.A. English, Low-dose neutron-irradiation damage in α-iron, J. Nucl. Mater. 108–109 (1982) 209–221. doi:10.1016/0022-3115(82)90489-5.
[67] M.L. Jenkins, Z. Yao, M. Hernández-Mayoral, M.A. Kirk, Dynamic observations of heavy-ion damage in Fe and Fe-Cr alloys, J. Nucl. Mater. 389 (2009) 197–202. doi:10.1016/j.jnucmat.2009.02.003.
[68] M. Matijasevic, W. Van Renterghem, A. Almazouzi, Characterization of irradiated single crystals of Fe and Fe–15Cr, Acta Mater. 57 (2009) 1577–1585. doi:10.1016/J.ACTAMAT.2008.11.042.
[69] M. Ruehle, M. Wilkens, Defocusing contrast of cavities, Cryst. Lattice Defects. 6 (1975) 129–140. https://inis.iaea.org/search/search.aspx?orig_q=RN:8303085 (accessed August 23, 2018).
[70] J. Schindelin, I. Arganda-Carreras, E. Frise, V. Kaynig, M. Longair, T. Pietzsch, S. Preibisch, C. Rueden, S. Saalfeld, B. Schmid, J.-Y. Tinevez, D.J. White, V. Hartenstein, K. Eliceiri, P. Tomancak, A. Cardona, Fiji: an open-source platform for biological-image analysis, Nat. Methods. 9 (2012) 676–682. doi:10.1038/nmeth.2019.
[71] J. Marian, B.D. Wirth, J.M. Perlado, Mechanism of Formation and Growth of Interstitial Loops in Ferritic Materials, Phys. Rev. Lett. 88 (2002) 255507. doi:10.1103/PhysRevLett.88.255507.
[72] B.C. Masters, Dislocation loops in irradiated iron, Philos. Mag. 11 (1965) 881–893. doi:10.1080/14786436508223952.
[73] K. Arakawa, M. Hatanaka, E. Kuramoto, K. Ono, H. Mori, Changes in the burgers vector of perfect dislocation loops without contact with the external dislocations, Phys. Rev. Lett. 96 (2006) 1–4. doi:10.1103/PhysRevLett.96.125506.
[74] R. Schäublin, B. Décamps, A. Prokhodtseva, J.F. Löffler, On the origin of primary ½ a0 and a0 loops in irradiated Fe(Cr) alloys, Acta Mater. 133 (2017) 427–439. doi:10.1016/J.ACTAMAT.2017.02.041.
[75] J.C. Haley, S.A. Briggs, P.D. Edmondson, K. Sridharan, S.G. Roberts, S. Lozano-Perez, K.G. Field, Dislocation loop evolution during in-situ ion irradiation of model FeCrAl alloys, Acta Mater. 136 (2017) 390–401. doi:10.1016/J.ACTAMAT.2017.07.011.
[76] Z. Yao, M. Hernández-Mayoral, M.L. Jenkins, M.A. Kirk, Heavy-ion irradiations of Fe and Fe–Cr model alloys Part 1: Damage evolution in thin-foils at lower doses, Philos. Mag. 88 (2008) 2851–2880. doi:10.1080/14786430802380469.
[77] F. Wan, Q. Zhan, Y. Long, S. Yang, G. Zhang, Y. Du, Z. Jiao, S. Ohnuki, The behavior of vacancy-type dislocation loops under electron irradiation in iron, J. Nucl. Mater. 455 (2014) 253–257. doi:10.1016/J.JNUCMAT.2014.05.048.
[78] G.S. Was, Z. Jiao, E. Getto, K. Sun, A.M. Monterrosa, S.A. Maloy, O. Anderoglu, B.H. Sencer, M. Hackett, Emulation of reactor irradiation damage using ion beams, Scr. Mater. 88 (2014) 33–36. doi:10.1016/j.scriptamat.2014.06.003.
[79] G.A. Cottrell, S.L. Dudarev, R.A. Forrest, Immobilization of interstitial loops by substitutional

alloy and transmutation atoms in irradiated metals, J. Nucl. Mater. 325 (2004) 195–201. doi:10.1016/J.JNUCMAT.2003.12.001.
[80] K. Arakawa, M. Hatanaka, H. Mori, K. Ono, Effects of chromium on the one-dimensional motion of interstitial-type dislocation loops in iron, J. Nucl. Mater. 329–333 (2004) 1194–1198. doi:10.1016/j.jnucmat.2004.04.263.
[81] M.R. Gilbert, S.L. Dudarev, P.M. Derlet, D.G. Pettifor, Structure and metastability of mesoscopic vacancy and interstitial loop defects in iron and tungsten, J. Phys. Condens. Matter. 20 (2008) 345214. doi:10.1088/0953-8984/20/34/345214.
[82] N. Soneda, S. Ishino, T.D. de la Rubia, Vacancy loop formation by “cascade collapse” in a-Fe: A molecular dynamics study of 50keV cascades, Philos. Mag. Lett. 81 (2001) 649–659. doi:10.1080/09500830110062799.
[83] R.E. Stoller, L.R. Greenwood, Subcascade formation in displacement cascade simulations: Implications for fusion reactor materials, J. Nucl. Mater. 271–272 (1999) 57–62. doi:10.1016/S0022-3115(98)00730-2.
[84] D.J. Bacon, F. Gao, Y.N. Osetsky, Primary damage state in fcc, bcc and hcp metals as seen in molecular dynamics simulations, J. Nucl. Mater. 276 (2000) 1–12. doi:10.1016/S0022-3115(99)00165-8.
[85] M.-C. Marinica, F. Willaime, J.-P. Crocombette, Irradiation-Induced Formation of Nanocrystallites with C15 Laves Phase Structure in bcc Iron, Phys. Rev. Lett. 108 (2012) 025501. doi:10.1103/PhysRevLett.108.025501.
[86] J. Chen, F. Duval, P. Jung, R. Schäublin, N. Gao, M.F. Barthe, Dislocation loops in ultra-high purity Fe(Cr) alloys after 7.2 MeV proton irradiation, J. Nucl. Mater. 503 (2018) 81–90. doi:10.1016/J.JNUCMAT.2018.02.042.
[87] A.H.M. Krom, A.D. Bakker, Hydrogen trapping models in steel, Metall. Mater. Trans. B Process Metall. Mater. Process. Sci. 31 (2000) 1475–1482. doi:10.1007/s11663-000-0032-0.
[88] A.R.C. Brouwer, R. Griessen, H. Wipf, Solubility and Diffusion of Hydrogen in Pure Metals and Alloys, Phys. Scr. T94 (2001) 43. doi:10.1238/Physica.Topical.094a00043.
[89] A. Caro, J. Hetherly, A. Stukowski, M. Caro, E. Martinez, S. Srivilliputhur, L. Zepeda-Ruiz, M. Nastasi, Properties of Helium bubbles in Fe and FeCr alloys, J. Nucl. Mater. 418 (2011) 261–268. doi:10.1016/j.jnucmat.2011.07.010.
[90] S.M.H. Haghighat, G. Lucas, R. Schäublin, State of a pressurized helium bubble in iron, EPL (Europhysics Lett. 85 (2009) 60008. doi:10.1209/0295-5075/85/60008.
[91] V. Kuksenko, C. Pareige, P. Pareige, Cr precipitation in neutron irradiated industrial purity Fe–Cr model alloys, J. Nucl. Mater. 432 (2013) 160–165. doi:10.1016/J.JNUCMAT.2012.07.021.
[92] M. Bachhav, G. Robert Odette, E.A. Marquis, Microstructural changes in a neutron-irradiated Fe–15at.%Cr alloy, J. Nucl. Mater. 454 (2014) 381–386. doi:10.1016/j.jnucmat.2014.08.026.
[93] E.R. Reese, M. Bachhav, P. Wells, T. Yamamoto, G. Robert Odette, E.A. Marquis, On α’ precipitate composition in thermally annealed and neutron-irradiated Fe- 9-18Cr alloys, J. Nucl. Mater. 500 (2018) 192–198. doi:10.1016/J.JNUCMAT.2017.12.036.
[94] F. Soisson, T. Jourdan, Radiation-accelerated precipitation in Fe–Cr alloys, Acta Mater. 103 (2016) 870–881. doi:10.1016/j.actamat.2015.11.001.
[95] O. Senninger, F. Soisson, E. Martínez, M. Nastar, C.-C. Fu, Y. Bréchet, Modelling radiation induced segregation in iron–chromium alloys, Acta Mater. 103 (2016) 1–11. doi:10.1016/J.ACTAMAT.2015.09.058.
[96] R. Cauvin, G. Martin, Solid solutions under irradiation. I. A model for radiation-induced metastability, Phys. Rev. B. 23 (1981) 3322–3332. doi:10.1103/PhysRevB.23.3322.
[97] O. Tissot, C. Pareige, E. Meslin, B. Décamps, J. Henry, Influence of injected interstitials on α’ precipitation in Fe–Cr alloys under self-ion irradiation, Mater. Res. Lett. 5 (2017) 117–123. doi:10.1080/21663831.2016.1230896.
[98] J.H. Ke, E.R. Reese, E.A. Marquis, G.R. Odette, D. Morgan, Flux effects in precipitation under irradiation – Simulation of Fe-Cr alloys, Acta Mater. 164 (2019) 586–601.

doi:10.1016/j.actamat.2018.10.063.

1045